UNIVERSITY OF CALIFORNIA
SANTA CRUZ

MODELING OF COASTAL AND ESTUARINE PROCESSES:
HYBRID STATISTICAL-DYNAMICAL PREDICTION OF NEARSHORE WAVES AND DYNAMICAL SIMULATION OF TIDAL FLOW IN IDEALIZED ESTUARINE EMBAYMENTS

A dissertation submitted in partial satisfaction
of the requirements for the degree of

DOCTOR OF PHILOSOPHY

in

OCEAN SCIENCES

by

Christie A. Hegermiller

September 2017

The Dissertation of Christie A. Hegermiller is approved:

____
Professor Christopher A. Edwards, chair

____
Professor Andrew M. Moore

____
Patrick L. Barnard, Ph.D.

____
Li H. Erikson, Ph.D.

____
Tyrus Miller
Vice Provost and Dean of Graduate Studies

TABLE OF CONTENTS

CHAPTER ONE: INTRODUCTION……………………………………………………1

CHAPTER TWO...…………………………………………………………….….15
A multimodal wave spectrum-based approach for statistical downscaling of local wave climate

CHAPTER THREE…………………………………………………………….28
Controls of multimodal wave conditions in a complex coastal setting

CHAPTER FOUR...……………………………………………………………53
Tidally-driven circulation of an idealized small, shallow estuarine embayment

CHAPTER FIVE: CONCLUSION……………………………………………...103

ABSTRACT

MODELING OF COASTAL AND ESTUARINE PROCESSES: HYBRID STATISTICAL-DYNAMICAL PREDICTION OF NEARSHORE WAVES AND DYNAMICAL SIMULATION OF TIDAL FLOW IN IDEALIZED ESTUARINE EMBAYMENTS

by

Christie A. Hegermiller

Climate change exerts physical influence on estuarine and open coastal morphology through sea level rise and changes to wave energy, precipitation, and sediment supply, resulting in flooding and erosion hazards to coastal communities.

Along open coasts, the distribution of wave energy in the nearshore is of critical importance for assessing local vulnerability to climate change. Two methods are frequently used to predict wave conditions based on global climate model outputs of atmospheric circulation: dynamical downscaling and statistical downscaling. Statistical downscaling relies on empirical relationships between waves and atmospheric conditions. Statistical downscaling has been applied with success in relatively small ocean basins (e.g., Mediterranean, Atlantic) where waves are generated over a small area and arrive at the coast within a few days of generation. However, in the Pacific Basin, waves are generated over large and distant regions of both the North and South Pacific. Furthermore, waves can travel up to 3 weeks before arriving at the coast (e.g., Southern Ocean-generated waves arriving in Southern California). These challenges have resulted in statistical downscaling studies with limited success. Chapter 2 of this dissertation addresses these challenges by 1) partitioning wave spectra into families that have unique, discrete generation areas and 2) accounting for the time lag between wave generation and wave arrival at the coast.

The success of this work in Southern California bodes well for the proliferation of wave climate projections in large ocean basins.

To project future coastal hazards, deep-water waves predicted using the methods described above must be transformed over shelf bathymetry to the nearshore. In complex coastal regions, offshore canyons, shoals, and islands complicate the linkage of nearshore waves to deep-water waves and the atmospheric conditions that generated them. In Chapter 3 of this dissertation, a hybrid statistical-dynamical approach is taken to explore significant spatial variability in nearshore wave conditions of the Southern California Bight, a complex coastal region. It is found that variability is driven by not only static bathymetric controls, but also dynamic large-scale atmospheric patterns. Climate change effects on these atmospheric patterns will lead to new distributions of wave energy along the Southern California Bight coastline and other coastlines around the world.

Along estuarine coasts, the distribution of tracers, such as salt, sediment, and pollutants, is a key factor in determining vulnerability to climate change and development. Extensive scientific effort has yielded a comprehensive understanding of sediment and salt transport in varied estuarine systems. However, tidal dynamics in shallow embayments, which are commonly found flanking deep estuarine channels, have not been described thoroughly. Chapter 4 of this dissertation examines the momentum and salt forcing associated with a shallow, estuarine embayment. This work illuminates mechanisms likely responsible for trapping of sediments in shallow bays and the supply of sediment to estuarine marshes.

The suite of studies presented in this dissertation seeks to contribute to our scientific understanding of open and estuarine coastal response to climate change and to provide information that can readily be applied to coastal policy and engineering.

ACKNOWLEDGEMENTS

Thank you to my trifecta of advisors, who each in his/her own way has guided me through the last five years. I cannot imagine a more skilled, enthusiastic, and wonderful group to teach me, from both scientific and personal perspectives.

- Thank you, Patrick, for your constant assurance and commitment, for always being open, and for letting me know that it's okay to have ups and downs. You have shown me how to approach the downs with grace, composure, and a plan.
- Thank you, Li, for every moment of patience that you have exercised with me, for letting me walk into your office just to say my thoughts out loud, and for helping me every step of the way. You have been my guiding light and my support beams.
- Thank you, Chris, for knowing when to push me and when to pull me back. You have the unique ability of finding the positive in everything, which was absolutely crucial during times of frustration. Thank you for very gracefully steering me in the right directions.

Thank you to Andy Moore for helpful and interesting discussion.

Thank you to the CI-CPT group at USGS and to my lab group at UCSC. Thank you to my colleagues at IH Cantabria and the University of Cantabria. I feel fortunate to work alongside of friends who are also brilliant resources. Thank you to Curt Storlazzi, Jessie Lacy, and Gary Griggs for mentorship, scientific discussion, and patience.

Thank you to my friends in Santa Cruz for bursting the limits of my life wide open. You turned this strange place into home. Thank you especially to SeanPaul and Ila for getting me outside, whether it's for a lunchtime ride or a weekend adventure.

Thank you to my best friends, Marissa and Victoria, for celebrating my successes and letting me express my failures, for supporting me and cheering me on, and for loving me unconditionally. You have been a source of happiness and laughter for nearly my whole life.

Thank you, Justin, for being the most wonderful person to come home to every day, for giving me balance, and for supporting me in so many ways. Everything is better with you, both the day-to-day adventures and our larger ones, of which there are many.

Thank you to my family.
Thank you, Robbie, for helping me to see new perspectives, both in life and in work.

Thank you, Mom, for supporting me from day one, for encouraging my passions whole-heartedly, and for believing in me. Thank you for all of the experiences you enabled that have lead to this moment. Thank you for encouraging my path even when it has taken me far from you and even when it is so different from the one you have taken.

Thank you, Dad, who guides me yet from the other dimensions and who loved the ocean.

The text of this dissertation includes reprints of the following previously published and submitted materials:

Hegermiller, C.A., J.A.A. Antolinez, A. Rueda, P. Camus, J. Perez, L.H. Erikson, P.L. Barnard, and F.J. Mendez, 2016. A multimodal wave spectrum-based approach for statistical downscaling of local wave climate. *Journal of Physical Oceanography*, 47, doi:10.1175/JPO-D-16-0191.1.

Hegermiller, C.A., A. Rueda, L.H Erikson, P.L. Barnard, J.A.A. Antolinez, and F.J. Mendez, submitted. Controls of multimodal wave conditions in a complex coastal setting. Submitted to *Geophysical Research Letters*.

The co-authors F.J. Mendez and P.L. Barnard listed in these publications and in supervised the research which forms the basis for this dissertation. The co-author L.H. Erikson directed the research which forms the basis of the second publication and provided technical direction and theoretical insight to the work. The co-authors A. Rueda, J.A.A. Antolinez, P. Camus, and J. Perez shared technical methodologies. A. Rueda and J. Perez provided results from their work on which to build the research.

CHAPTER ONE
INTRODUCTION

Coastal zones are of significant social, economic, and environmental importance. Coastal zones can be defined as areas below 10 m elevation with hydrologic connection to the ocean, encompassing both open and estuarine coastlines (Neumann et al., 2015). At present, more than 600 million people live in coastal zones worldwide (McGranahan et al., 2007). Coastal areas experience larger population growth than inland areas and migration to coastal cities continues globally (Hugo, 2007). As a result, global coastal populations are expected to more than double over the next century (Neumann et al., 2015). Critical infrastructure concentrated along coasts will need to expand to accommodate increasing populations (Melillo et al., 2014). In addition to social importance, coastal zones are of substantial economic value as well, as coastal populations contribute half of the world gross domestic product (Kummu et al., 2016). Lastly, ecosystem services, such as fisheries habitat, water filtration, erosion control, and coastal protection, provided by coastal systems deliver further benefits that are more difficult to quantify (Barbier et al., 2011).

Rapid and increasing socioeconomic development yields extensive anthropogenic impacts to coastal regions (Nicholls et al., 2008). Estuarine and open coast environments experience deterioration associated with direct human use and indirect human influences. Direct impacts include land use change through development, land extension by marsh infilling, pollution, resource extraction and dredging, and reduction of water and sediment flow to the ocean through damming (Barnard et al., 2013). Along open coasts, further impacts include development up to or on beaches and cliffs, construction of hard structures for protection, and beach nourishment. The largest indirect influence is anthropogenic climate change, which diminishes the social, economic, and environmental value of estuarine and coastal systems over human time scales. Changes to global and regional atmosphere-ocean conditions due to climate change exert physical influences on coastal morphology and biogeochemical influences on coastal ecosystems.

At the open coast, coastal flooding (Barnard et al., 2014), shoreline retreat (Ruggiero et al., 2001), and groundwater salinization (Hoover et al., 2016) threaten communities over event-based to multi-decadal timescales. Coastal flooding results from the combination of sea level rise (SLR), high tides (Sweet et al., 2014), storm surge induced by sea level pressure and wind forcing, sea level anomalies related to low-frequency atmosphere-ocean oscillations (Enfield and Allen, 1980), and wave runup during extreme storms (Stockdon et al., 2006). Shoreline change by cliff and beach erosion is driven by direct wave impact and cross-shore and alongshore transport of sediment. For decades, SLR has been the focus of coastal communities seeking to mitigate climate change-driven coastal hazards. Ice melt and water expansion due to temperature increases induce SLR, which is currently at a rate of 3-4 mm/yr (Watson et al., 2015; Yi et al., 2015) with significant global spatial variability due to vertical land motions and local dynamical suppression or enhancement of SLR by winds and ocean circulation (Reid and Mantyla, 1976; Bromirski et al., 2011). Projections for SLR over the 21st century range from 0.3-2.0 m (Horton et al., 2014), though recent work suggests significant underprediction of rates of ice sheet collapse, implying that the upper limits of SLR over the 21st century are larger than current projections (DeConto and Pollard, 2016). In light of extensive coastal vulnerability due to SLR, Vitousek et al. (2017) demonstrated that the effects of storm surge and wave runup double the frequency of coastal flooding projected for 2050 by SLR alone. Increasingly, coastal managers and engineers seek rigorous projections of future wave conditions to anticipate and address additional coastal vulnerability due to changes in waves.

Changes to temperature gradients across Earth over the next century and beyond alter atmospheric pressure distributions, which regulates the frequency and magnitude of extreme and mean wind and wave conditions (Hemer et al., 2013). The standard tools for projection of climate variables, such as temperature and precipitation, into the future are global climate models (GCM), which allow us to integrate knowledge gained from observational records into dynamical predictions of future Earth systems. Increased complexity of GCMs and increased computational power over recent decades have yielded a powerful capability. GCMs enable prediction of climate variables, exploration of their nonlinear relationships and underlying mechanisms, and performance of future climate experiments. Uncertainty in predictions accompanies our incomplete understanding of the climate system, particularly atmospheric dynamics, ice sheet dynamics, and global teleconnections (Stevens and Bony, 2013; Sherwood et al., 2014). Nonetheless, the ensemble of GCMs developed at various institutions around the world statistically represents our best projection given the state of the art.

Generation of ocean surface gravity waves by near-surface winds is not yet dynamically simulated or parameterized within GCMs, though this is an active area of research (Hemer et al., 2012). Two methods, each with benefits and drawbacks, exist to project future waves from GCM fields to spatial scales of use to coastal managers and engineers (Giorgi et al., 2001; Camus et al., 2011). Both downscaling methods predict waves at relatively high resolutions over relatively small spatial scales compared to the large-scale forcing. The first is dynamical downscaling, in which wave growth, propagation, and decay are simulated using a physics-based numerical model forced by space- and time-varying near-surface winds (e.g., Hemer et al., 2013; Erikson et al., 2015). Dynamical downscaling describes wave processes and nonlinear interactions between waves in both frequency and direction space. However, this method is computationally expensive, especially when generating ensemble predictions over long time periods. As a result, the majority of studies using dynamical downscaling to project waves are limited in the number of GCMs or climate scenarios considered (e.g., Mori et al., 2010; Erikson et al., 2015).

The second method to project future waves is statistical downscaling, which relies on the statistical relationships between variables of regional atmospheric circulation, such as sea level pressure or winds, and variables of local wave conditions, such as significant wave height, period, direction, or the full directional spectrum (e.g., Wang et al., 2010; Graham et al., 2012; Mori et al., 2013; Camus et al., 2014; Wang et al., 2014). Statistical downscaling is computationally efficient and allows for simultaneous characterization and projection of atmospheric patterns and wave conditions. However, its success is limited by the quality and quantity of data available and the definition of the predictor (atmosphere) and predictand (waves). In large ocean basins, such as the Pacific Ocean, waves are generated by winds in disparate, discrete areas and travel days to weeks before arriving at the coasts. As a result, the directional wave spectrum exhibits multiple wave energy peaks, with waves generated both locally and in distant regions. This multimodality introduces difficulty in forming statistical relationships between atmospheric and wave conditions (Espejo et al., 2014). Chapter 2 of this dissertation presents an improved methodology to statistically downscale multimodal wave conditions from regional atmospheric patterns by linking wave spectral peaks with discrete generation regions and by integrating a time dependency to account for differences in propagation time across large ocean basins (Hegermiller et al., 2016). The method is tested successfully for the deep-water wave climate of Southern California.

In complex coastal areas, deep-water wave conditions are not sufficient for prediction of coastal hazards because waves are transformed considerably across complex shelf systems. Deep-water waves are refracted over bathymetry, including shoals and canyons, and shadowed and diffracted by offshore islands. As a result, the nearshore wave climate of a complex coastal area can exhibit high spatial variability, meaning that neighboring coasts are sensitive to different atmospheric patterns. Chapter 3 employs a new statistical-dynamical method to characterize the contributions to nearshore wave energy flux of waves generated in different parts the ocean basin (Hegermiller et al., submitted). The method allows for detailed analysis of the variability of nearshore wave forcing along a contiguous coast in light of projected climate change. The applicability of the method to complex coastal areas is demonstrated for the Southern California Bight, built on results from Chapter 2 (Hegermiller et al., 2016; Rueda et al., 2017).

Coastal hazards exist in estuarine environments as well. Intensive human use of estuaries coupled with typical circulation patterns result in the common configuration of deep channels flanked by shallow shoals, embayments, and marshes. SLR and reduction to water and sediment flow by damming, dredging, or climate change threaten estuarine coasts (Ranasinghe et al., 2012). Estuarine marshes rely on mud and fine sand supplied by circulation patterns to maintain their elevation with respect to SLR (BCDC and ESA PWA, 2013). The distribution of salt and sediment within estuaries governs the distribution of fish and mollusk species and changes to these variables will determine suitable habitat in the future. Lastly, contaminants can bind to muddy sediments. In this case, sediment acts as a vehicle for estuary contamination. Understanding the physical mechanisms responsible for the transport of tracers, such as salt, sediment, and contaminants, is important for focused restoration efforts, improved regulation and policy, and mitigation of future coastal impacts.

Estuarine environments vary widely over the Earth, as do the physical processes that dominate in them (Valle-Levinson, 2010). Significant scientific effort has focused on understanding these processes. Estuarine circulation in the along-channel direction has been well-described by both observational and modeling studies

(Hansen and Rattray, 1965; Geyer and MacCready, 2014). In estuarine environments where river forcing is important, along-channel distributions of salt introduce an along-channel pressure gradient and large velocities during tidal phases introduce vertical mixing. The balance between these two forces results in an along-channel estuarine circulation in which saltwater flows into the estuary from the ocean at the bottom of the channel, while freshwater exits the river at the surface (Hansen and Rattray, 1965). The estuarine circulation is an effective trapping mechanism for sediment and other tracers. Recent work has challenged the dynamical description of estuarine circulation. In some estuaries, across-channel and vertical advection of momentum become dominant, though the resulting circulation is the same.

Circulation in the across-channel direction is developed by the Coriolis force, channel curvature, and across-channel density gradients driven by salinity (Lerczak and Geyer, 2004). Across-channel salinity gradients can be set up by the across-channel distribution of along-channel flow, which transports salt different along-channel distances depending on across-channel location (Nunes and Simpson, 1985). Across-channel salinity gradients can also be generated by boundary mixing over a sloping bottom (Chen and Sanford, 2009). Both channel curvature and Coriolis forcing yield flow veering and asymmetries in the across-channel direction. Across-channel circulation can be locally generated at bathymetric features, such as islands, headlands, and shoals. Across-channel flows are important for the transport of mobile pools of sediment and salt over short time scales, however they also influence along-channel circulation, channel evolution, and biological communities over longer time scales.

In Chapter 4, a numerical model is used to explore the transport of salt from the deep channel to shallow flanks in an idealized, small estuarine embayment. The embayment geometry mimics that of a small bay in San Francisco Bay that is the focus of local restoration efforts (Lacy and Hoover, 2011). This work investigates eddy formation associated with tidal flow past embayments, built on collective knowledge of along- and across-channel circulation described above, and the response of the embayment to the evolution of the channel. Results from Chapter 4 contribute to the understanding of dynamics crucial for marsh sustainability in the face of SLR and other human influences.

Though California's coastline is the focal point of Chapters 2 and 3, open coast and estuarine response to changing physical conditions as a result of anthropogenic influences is applicable to coastal communities across the world. Research presented in Chapters 2 and 3 identifies systematic methodologies for projecting wave conditions and coastal sensitivity in light of climate change, which can be applied to most coastal settings. Research presented in Chapter 4 examines transport in an idealized estuarine embayment, which sheds light on mechanisms governing vulnerability of estuaries to human influences worldwide.

REFERENCES

Barbier, E.B., S.D. Hacker, C. Kennedy, E.W. Koch, A.C. Stier, and B.R. Silliman, 2011. The value of estuarine and coastal ecosystem services. *Ecological Monographs*, **81**, 169-193.

Barnard, P.L., D.H. Schoellhamer, B.E. Jaffe, and L.J. McKee, 2013. Sediment transport in the San Francisco Bay Coastal System: An overview. *Marine Geology*, **345**: 3-17.

Barnard, P.L., M. van Ormondt, L.H. Erikson, J. Eshleman, C. Hapke, P. Ruggiero, P.N. Adams, and A.C. Foxgrover, 2014. Development of the Coastal Storm Modeling System (CoSMoS) for predicting the impact of storms on high-energy, active-margine coasts. *Natural Hazards*, **74**, 1095-1125, doi:10.1007/s11069-014-1236-y.

Bromirski, P.D., A.J. Miller, R.E. Flick, and G. Auad, 2011. Dynamical suppression of sea level rise along the Pacific coast of North America: Indications for imminent acceleration. *Journal of Geophysical Research: Oceans*, **116**, doi:10.1029/2010JC006759.

Camus, P., M. Menendez, F.J. Mendez, C. Izaguirre, A. Espejo, V. Canovas, J. Perez, A. Rueda, I.J. Losada, and R. Medina, 2014. A weather-type statistical downscaling framework for ocean wave climate. *Journal of Geophysical Research: Oceans*, 119, 7389-7405.

Chen, S.N. and L.P. Sanford, 2009. Lateral circulation driven by boundary mixing and the associated transport of sediments in Idealized partially mixed estuaries. *Continental Shelf Research*, 29, 101-118, doi:10.1016/j.csr.2008.01.001.

DeConto, R.M. and D. Pollard, 2016. Contribution of Antarctica to past and future sea-level rise. *Nature*, **531**, 591-597, doi:10.1038/nature17145.

Enfield, D.B. and J.S. Allen, 1980. On the structure and dynamics of monthly mean sea level anomalies along the Pacific coast of North and South America. *Journal of Physical Oceanography*, **10**.

Erikson, L.H. C.A. Hegermiller, P.L. Barnard, P. Ruggiero, and M. van Ormondt, 2015. Projected wave conditions in the Eastern North Pacific under the influence of two CMIP5 climate scenarios. *Ocean Modelling*, **96**, 171-185, doi:10.1016/j.ocemod.2015.07.004.

Espejo, A., P. Camus, I.J. Losada, and F.J. Mendez, 2014. Spectral ocean wave climate variability based on atmospheric circulation patterns. *Journal of Physical Oceanography*, doi:10.1175/JPO-D-13-0276.1.

Geyer, W.R. and P. MacCready, 2014. The estuarine circulation. *Annual Review of Fluid Mechanics*, **46**, doi:10.1146/annurev-fluid-010313-141302.

Giorgi, F., B. Hewitson, J. Christensen, M. Hulme, H. von Storch, P. Whetton, R. Jones, L. Mearns, and C. Fu, 2001. Regional climate information – Evaluation and projections. In *Climate Change 2001. The Scientific Basis. Contribution of Working Group to the Third Assessment Report of the IPCC: Contribution to Working Group I*, edited by J.T. Houghton et al., chap. 10, 583-638. Cambridge Univ. Press, Cambridge, U.K.

Hansen, D.V. and M. Rattray, 1965. Gravitational circulation in straits and estuaries. *Journal of Marine Research*, 23, 104-122.

Hegermiller, C.A., J.A.A. Antolinez, A. Rueda, P. Camus, J. Perez, L.H. Erikson, P.L. Barnard, and F.J. Mendez, 2016. A multimodal wave spectrum-based approach for statistical downscaling of local wave climate. *Journal of Physical Oceanography*, doi:10.1175/JPO-D-16-0191.1.

Hegermiller, C.A., A. Rueda, L.H. Erikson, P.L. Barnard, J.A.A. Antolinez, and F.J. Mendez, submitted. Controls of multimodal wave conditions in a complex coastal setting.

Hemer, M.A., X.L. Wang, R. Weisse, and V.R. Swail, 2012. Advancing wind-waves climate science: the COWCLIP project. *Bulletin of the American Meteorological Society*, doi:10.1175/BAMS-D-11-00184.1.

Hemer, M.A., Y. Fan, N. Mori, A. Semedo, and X.L. Wang, 2013. Projected changes in wave climate from a multi-model ensemble. *Nature Climate Change*, **3**, 471-476, doi:10.1038/nclimate1791.

Hoover, D.J., K.O. Odigie, P.W. Swarzenski, and P.L. Barnard, 2016. Sea-level rise and coastal groundwater inundation and shoaling at select sites in California, USA. *Journal of Hydrology: Regional Studies*, doi:10.1016/j.ejrh.2015.12.055.

Horton, B.P., S. Rahmstorf, S.E. Englehard, and A.C. Kemp, 2014. Expert assessment of sea-level rise by AD 2100 and AD 2300. *Quaternary Science Reviews*, **84**, doi:10.1016/j.quascirev.2013.11.002.

Hugo G., 2011. Future demographic change and its interactions with migration and climate change. *Global Environmental Change*, **21**.

Kummu, M., H. de Moel, G. Salvucci, D. Viviroli, P.J. Ward, and O. Varis, 2016. Over the hills and further away from coast: global geospatial patterns of human and environment over the 20th-21st centuries. *Environmental Research Letters*, **11**, doi:10.1088/1748-9326/11/3/034010.

Lacy, J.R. and D.J. Hoover, 2011. Wave exposure of Corte Madera Marsh, Marin County, California – a field investigation. U.S. Geological Survey Open-File Report 2011-1183.

Lerczak, J.A. and W.R. Geyer, 2004. Modeling the lateral circulation in straight, stratified estuaries. *Journal of Physical Oceanography*, 34, 1410-1428.

McGranahan, G., D. Balk, and B. Anderson, 2007. The rising tide: assessing the risks of climate change and human settlements in low elevation coastal zones. *Environment and Urbanization*, **19**, 17-37.

Melillo, J.M., T.C. Richmond, and G.W. Yohe, 2014. Climate change impacts in the United States: The third national climate assessment. U.S. Global Change Research Program. doi:10.7930/J0Z31WJ2.

Mori, N., T. Yasuda, H. Mase, T. Tom, and Y. Oku, 2010. Projection of extreme wave climate change under global warming. *Hydrological Research Letters*, **4**, 15-19.

Mori, N., T. Shimura, T. Yasuda, and H. Mase, 2013. Multi-model climate projections of ocean surface variables under different climate scenarios – Future change of waves, sea level and wind. *Ocean Engineering*, **71**, 122-129.

Neumann, B., A.T. Vafeidis, J. Zimmermann, and R.J. Nicholls, 2015. Future coastal population growth and exposure to sea-level rise and coastal flooding - A global assessment. *PLoS ONE*, **10**, doi:10.1371/journal.pone.0118571.

Nicholls, R.J., P.P. Wong, V. Burkett, C.D. Woodroffe, and J. Hay, 2008. Climate change and coastal vulnerability assessment: scenarios for integrated assessment. *Sustainability Science*, **3**, 89-102.

Nunes, R.A. and J.H. Simpson, 1985. Axial convergence in a well-mixed estuary. *Estuarine Coastal Shelf Science*, 20, 637-649.

Ranasinghe, R., T.M. Duong, S. Uhlenbrook, D. Roelvink, and M. Stive, 2012. Climate-change impact assessment for inlet-interrupted coastlines. *Nature Climate Change*, doi:10.1038/nclimate1664.

Reid, J.L. and A.W. Mantyla, 1976. The effect of the geostrophic flow upon coastal sea elevations in the northern North Pacific Ocean. *Journal of Geophysical Research*, **81**, doi:10.1029/JC081i018p03100.

Rueda, A., C.A. Hegermiller, J.A.A. Antolinez, P. Camus, S. Vitousek, P. Ruggiero, P.L. Barnard, L.H. Erikson, A. Tomas, and F.J. Mendez, 2017. Multiscale climate emulator of multimodal wave spectra: MUSCLE-spectra. *Journal of Geophysical Research: Oceans*, **122**, doi:10.1002/2016JC011957.

Ruggiero, P., P.D. Komar, W.G. McDougal, J.J. Marra, and R.A. Beach, 2001. Wave runup, extreme water levels and the erosion of properties backing beaches. *Journal of Coastal Research*, 407-419.

San Francisco Bay Conservation and Development Commission and ESA PWA, 2013. Corte Madera Baylands: Conceptual Sea Level Rise Adaptation Strategy.

Sherwood, S.C., S. Bony, and J.L. Dufresne, 2014. Spread in model climate sensitivity traced to atmospheric convective mixing. *Nature,* **505**, 37-42, doi:10.1038/nature12829.

Stevens, B. and S. Bony, 2013. What are climate models missing? *Science*, **340**, 1053-1054, doi:10.1126/science.1237554.

Stockdon, H.F., R.A. Holman, P.A. Howd, and A.H. Sallenger, 2006. Empirical parameterizations of setup, swash, and runup. *Coastal Engineering*, **53**(7), 573-588, doi:10.1016/j.coastaleng.2005.12.005.

Sweet, W., J. Park, J. Marra, C. Zervas, and S. Gill, 2014. Sea level rise and nuisance flood frequency changes around the United States. *NOAA Technical Report NOS CO-OPS 073*.

Valle-Levinson, A., 2010. Definition and classification of estuaries. In *Contemporary Issues in Estuarine Physics*, ed. A Valle-Levinson, 1-11. Cambridge Univ. Press, Cambridge, U.K.

Vitousek, S., P.L. Barnard, C.H. Fletcher, N. Frazer, L.H. Erikson, and C.D. Storlazzi, 2017. Doubling of coastal flooding frequency within decades due to sea-level rise. *Nature Scientific Reports*, **7**, 1399, doi:10.1038/s41598-017-01362-7.

Wang, X.L., V.R. Swail, and A. Cox, 2010. Dynamical *versus* statistical downscaling methods for ocean wave heights. *International Journal of Climatology*, **30**, 317-332.

Wang, X.L., Y. Feng, and V.R. Swail, 2014. Changes in global ocean wave heights as projected using multimodel CMIP5 simulations. *Geophysical Research Letters*, **41**(3), 1026-1034.

Watson, C.S., N.J. White, J.A. Church, M.A. King, R.J. Burgette, and B. Legresy, 2015. Unabated global mean sea-level rise over the satellite altimeter era. *Nature Climate Change*, **5**, 565-568, doi:10.1038/nclimate2635.

Yi, S., W. Sun, K. Heki, and A. Qian, 2015. An increase in the rate of global mean sea level rise since 2010. *Geophysical Research Letters*, **42**, doi:10.1002/2015GL063902.

CHAPTER TWO
A MULTIMODAL WAVE SPECTRUM-BASED APPROACH FOR STATISTICAL DOWNSCALING OF LOCAL WAVE CLIMATE

A Multimodal Wave Spectrum–Based Approach for Statistical Downscaling of Local Wave Climate

C. A. Hegermiller

Department of Ocean Sciences, University of California, and Pacific Coastal and Marine Science Center, United States Geological Survey, Santa Cruz, California

J. A. A. Antolinez and A. Rueda

Departamento Ciencias y Tecnicas del Agua y del Medio Ambiente, Universidad de Cantabria, Santander, Spain

P. Camus and J. Perez

Environmental Hydraulics Institute, Universidad de Cantabria, Santander, Spain

L. H. Erikson and P. L. Barnard

Pacific Coastal and Marine Science Center, United States Geological Survey, Santa Cruz, California

F. J. Mendez

Departamento Ciencias y Tecnicas del Agua y del Medio Ambiente, Universidad de Cantabria, Santander, Spain

(Manuscript received 17 August 2016, in final form 28 November 2016)

ABSTRACT

Characterization of wave climate by bulk wave parameters is insufficient for many coastal studies, including those focused on assessing coastal hazards and long-term wave climate influences on coastal evolution. This issue is particularly relevant for studies using statistical downscaling of atmospheric fields to local wave conditions, which are often multimodal in large ocean basins (e.g., Pacific Ocean). Swell may be generated in vastly different wave generation regions, yielding complex wave spectra that are inadequately represented by a single set of bulk wave parameters. Furthermore, the relationship between atmospheric systems and local wave conditions is complicated by variations in arrival time of wave groups from different parts of the basin. Here, this study addresses these two challenges by improving upon the spatiotemporal definition of the atmospheric predictor used in the statistical downscaling of local wave climate. The improved methodology separates the local wave spectrum into ''wave families,'' defined by spectral peaks and discrete generation regions, and relates atmospheric conditions in distant regions of the ocean basin to local wave conditions by incorporating travel times computed from effective energy flux across the ocean basin. When applied to locations with multimodal wave spectra, including Southern California and Trujillo, Peru, the new methodology improves the ability of the statistical model to project significant wave height, peak period, and direction for each wave family, retaining more information from the full wave spectrum. This work is the base of statistical downscaling by weather types, which has recently been applied to coastal flooding and morphodynamic applications.

1. Introduction

At a given time, the wave state of the ocean surface is a composite of wind seas and swell. Wind seas are generated by and strongly coupled with local winds, whereas swell is generated remotely and might have propagated over large distances. Though multiple definitions exist, swell can be distinguished from wind seas when the wave phase speed exceeds the overlaying wind speed by 20% (Semedo et al. 2011). Swells and seas are functions of both the intensity and frequency of atmospheric systems (Young et al. 2011). The wave state of the ocean surface represents a multitude of wind seas and swell trains, which each have a particular set of bulk wave statistics (significant wave height H_s, peak wave

Corresponding author e-mail: C. A. Hegermiller, chegermiller@usgs.gov

DOI: 10.1175/JPO-D-16-0191.1

period T_p, mean wave direction D_m, and directional spreading σ). Often, the wave spectrum exhibits multiple wave energy peaks (e.g., California deep-water wave climate; Crosby et al. 2016), with contributions of energy generated locally and energy propagated from distant regions. However, using the full wave spectrum from numerical wave models or wave buoys produces large volumes of data that pose management and analysis challenges. As a result, many studies examine bulk wave parameters of the largest energy peak of a spectrum while virtually eliminating secondary spectral peaks, which leads to incomplete and potentially misleading results. Recent advances allow for simple statistical representation of multimodal wave spectra but have yet to be widely applied (Portilla-Yandún et al. 2015).

Statistical downscaling methods for projecting local wave climate exploit the relationship between wave conditions and the magnitude and frequency of atmospheric systems. Statistical downscaling defines a linear (Wang et al. 2010) or nonlinear (this study) relationship between atmospheric variables, such as sea level pressure or wind speed, and wave parameters. These methods can be compared to dynamical downscaling, where a numerical wave model is forced by spatiotemporally varying winds (Erikson et al. 2015). Though statistical downscaling methods have been applied extensively with success in the Atlantic Ocean and Mediterranean Sea (Wang et al. 2012; Laugel et al. 2014; Camus et al. 2014a; Rueda et al. 2016a), the ability to use these methods in larger ocean basins (e.g., Pacific Ocean) is still being explored (Graham et al. 2013; Camus et al. 2014a; Rueda et al. 2017). Statistical downscaling relies on the quality of the definitions of the predictor (e.g., regional sea level pressure) and predictand (e.g., local wave conditions). One commonly used method for defining these fields is presented in Camus et al. (2014a). In that work, daily regional sea level pressure (SLP) fields averaged over an optimal number of days defined the predictor for daily total bulk wave parameters at a particular location (predictand). The spatial range of the predictor encompassed the primary areas of wave generation for the location, identified using Evaluating the Source and Travel Time of the Wave Energy Reaching a Local Area (ESTELA; Perez et al. 2014). The temporal range of the predictor was the average travel time of wave energy generated inside the wave generation region to the location, also identified using ESTELA.

In smaller ocean basins, such as the North Atlantic Ocean and Mediterranean Sea, the region of wave generation is relatively small. Thus, the travel times of wave energy generated within the basin (i.e., far from the location versus close to the location) differ by only a few days, usually less than 5 days. Additionally, wave spectra are often unimodal, with swell arriving from one discrete generation region. In these cases, the definition of the predictor and predictand following Camus et al. (2014a) is successful in reproducing historical or projecting future wave climates. However, in large ocean basins, such as the Pacific Ocean, the spatial and temporal definitions of the predictor and total bulk parameter definition of the predictand yield less successful statistical downscaling results. The reasons are twofold. First, waves may be generated in multiple discrete generation regions, yielding mixed sea states of local seas and multiple swell trains. Total bulk parameters and a single wave generation region do not adequately represent the wave climate. Second, travel times of wave energy generated in different parts of the region may differ by a few weeks. As a result, sea level pressure fields averaged over a time period do not physically relate to waves arriving on a particular day. In this work, we seek to improve the definitions of the predictor and predictand of Camus et al. (2014a) by 1) introducing ''wave families'' to better model multimodal spectra and multiple wave generation regions and 2) using isochrones of travel time to account for the vastness of wave generation regions.

The improved methodology is presented by defining the predictor and predictand for a location offshore of Southern California. Local wave conditions along Pacific coastlines are influenced by waves generated and propagated over very large distances, often the entire extent of the Pacific basin (Adams et al. 2008). Waves generated by distant storms in the central and western North Pacific and those generated in the South Pacific and Southern Ocean contribute to the bimodal wave spectrum of California (Crosby et al. 2016), making it difficult to form statistical relationships between atmospheric conditions and waves using existing methodologies for the reasons identified above (Espejo et al. 2014). The success of statistical downscaling for use in large ocean basins would allow for a more rapid proliferation of regional projections using numerous global climate models and forcing scenarios, creating an ensemble that would better estimate future wave conditions (Perez et al. 2015). Additionally, recent advances in statistical downscaling allow for simulation and projection of extreme bulk parameters, such as daily maximum significant wave height (Rueda et al. 2016a), coastal flooding (Rueda et al. 2016b), and coastal morphodynamics (Antolinez et al. 2016).

In this work, an improved methodology for defining the optimal predictor for statistical downscaling of multivariate (H_s, T_p, and D_m), multimodal wave climatology is presented, built on the methodology defined in

Camus et al. (2014a). Wind speed, SLP, and fetch are common variables used in predictor definitions for waves (Wang et al. 2010). Though near-surface winds are the drivers of wave growth, SLP and squared gradients of SLP fields contain information of both wind direction and magnitude, with spacing of isobars describing wind speed and orientation of isobars describing wind direction (Espejo et al. 2014). The methodology presented here utilizes the relationship between SLP and wave parameters while improving the ability to represent multimodal wave climates through wave families and incorporating physical intuition into the temporal and spatial definition of the predictor by using isochrones of travel time. The paper is structured as follows: Data and methods are presented in sections 2–5 through an application to Southern California, followed by an additional application to Trujillo, Peru, in section 6. This work concludes with brief comments in section 7.

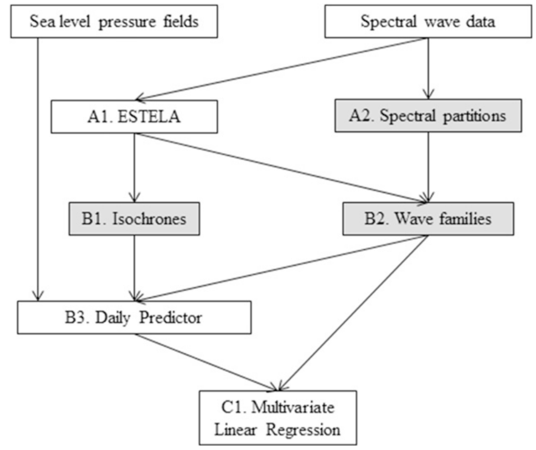

FIG. 1. Flowchart of the general methodology to define the optimal predictor for statistical downscaling of multimodal wave climate. Improvements to the Camus et al. (2014a) definition of the predictor are highlighted.

2. Methodology and data

Statistical downscaling defines a relationship between a predictor, here daily sea level pressure and the spatial gradients of sea level pressure, and a predictand, here daily multivariate wave parameters for multiple wave families at a particular location. This work seeks to improve the ability to statistically model multimodal wave climate. The methodology (Fig. 1) can be separated into three broad steps: step A, parameterization of spectral data; step B, spatiotemporal definition of the predictor; and, step C, a multiple multivariate linear regression model to assess the relationship between the variables. These steps are subdivided as follows.

- A1: Identify wave generation areas using ESTELA (Perez et al. 2014).
- A2: Partition the wave spectral data into sea and swell components.
- B1: Define the temporal range of the predictor using isochrones.
- B2: Identify wave families using wave generation areas and sea and swell partitions.
- B3: Construct a daily predictor of SLP for each wave family using the isochrones to create a temporal relationship between atmospheric fields and waves.
- C1: Use multiple multivariate linear regression analysis to assess the skill of the predictor to reproduce the predictand (daily wave conditions for each family).

The methodology is applied to a location in deep water off the coast of Southern California, United States (33°N, 120°W), as a demonstrative tool.

The historical SLP data used for statistical downscaling in this work were extracted from the National Centers for Environmental Prediction's Climate Forecast System Reanalysis (CFSR) dataset (Saha et al. 2010). CFSR SLP data are available at 6-hourly resolution from 1979 to 2009 on a 0.5° global grid. A global ocean wave reanalysis provided hourly directional wave spectra for the period 1979–2009 on a 1.5° longitude × 1° latitude global grid (Perez et al. 2015). To generate this reanalysis, the third-generation spectral wave model WAVEWATCH III (WW3; Tolman 2009) was forced at a global scale by CFSR near-surface winds. Bathymetry and shoreline data were populated with ETOPO1 (Amante and Eakins 2009) and National Geophysical Data Center Global Self-Consistent, Hierarchical, High-Resolution Shoreline (Wessel and Smith 1996). Wave spectra were computed with 15° directional resolution and 32 frequency bins ranging nonlinearly from 0.0372 to 0.714 Hz with a factor of 1.1.

3. Parameterization of spectral data

a. Wave generation areas

Wave climate along the California coast is a function of locally generated seas and swell generated in the North and South Pacific (Wingfield and Storlazzi 2007). To minimize the study area, a method developed by Perez et al. (2014) is used to identify the areas of wave generation contributing to local wave conditions at the particular location of interest. The method is referred to as ESTELA and uses geographic

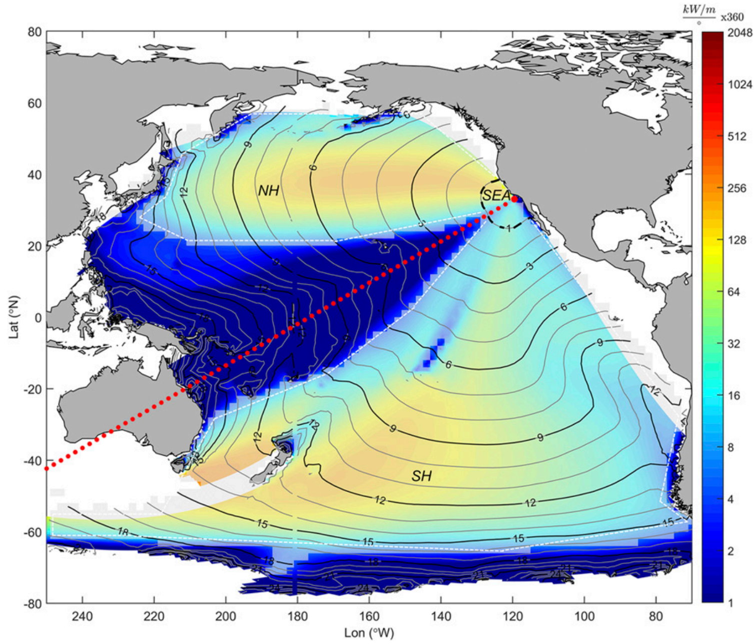

FIG. 2. ESTELA effective wave energy flux (color bar) for the location (large red dot) offshore of Southern California. The gray shading over the ocean, outlined generally in white dashed lines, denotes a threshold of 2 kW $m^{-1} {}^{\circ -1}$ imposed to define important wave generation regions. The isochrones of travel time are gray and black lines, with every third isochrone labeled in days. The red dotted line emanating from the location shows the demarcation of 240° for North and South Pacific swell families. The shaded area above the red dotted line is the spatial definition of the North Pacific swell family predictor (NH). The shaded area below the red dotted line is the spatial definition of the South Pacific swell family predictor (SH). The shaded area inside of the 1-day isochrone (black dashed line) is the SEA.

criteria and two-dimensional wave spectra to map areas of wave generation for a target point.

ESTELA reduces computational expenses by eliminating global grid cells that are blocked from the target point by landmasses, assuming that swell waves propagate along great circle paths (Snodgrass et al. 1966). A full discussion of the methodology and limitations can be found in Perez et al. (2014). Most importantly, ESTELA provides an estimate of the average effective energy flux toward the target point and the average travel time.

The ESTELA effective wave energy flux map for the location offshore of Southern California reveals two discrete wave energy generation regions: the North Pacific and an area in the western South Pacific near Australia and New Zealand (Fig. 2). These wave generation regions will contribute to the definition of the wave families. The travel times of wave energy reveal the time scales of wave propagation in the Pacific basin. Maximum travel time for swell generated in the North Pacific is 18 days, while the maximum travel time for swell generated in the South Pacific is 21 days (Fig. 2). Large differences in energy travel times across the basin (e.g., North Pacific swell arriving in 3 days generated in the eastern North Pacific and North Pacific swell arriving in 12 days generated in the western North Pacific) inspired improvements to the temporal definition of the predictor of Camus et al. (2014a).

b. *Wave spectral partitions*

Camus et al. (2014a) defined the statistical predictand as daily bulk wave parameters (e.g., H_s), but the information of the full, directional wave spectrum is critical for areas affected by multimodal wave climates. To efficiently represent multimodal wave conditions, energy of the full directional wave spectra is split into three partitions. Spectral partitions were defined using an algorithm adapted from terrestrial watershed delineation (Hanson and Jensen 2004). Local seas (zeroth partition) were identified as energy traveling in directions consistent with concurrent wind directions with a wave speed less than 1.5 times that of the wind speed, and two swell partitions were identified by condensing the energy surrounding spectral peaks. The first and second partitions compose wave energy from the dominant and secondary swell bands, respectively. Bulk wave parameters for each of these three spectral partitions were saved hourly on a global scale, such that wave conditions at a location are defined by ($H_{s0}, T_{p0}, D_{m0}, H_{s1}, T_{p1}, D_{m1}, H_{s2}, T_{p2}, D_{m2}$). It is important to note that this partitioning algorithm does not use a cutoff frequency to differentiate between seas and swell but instead characterizes seas and swell based on the ratio of wave and wind speeds. Portilla-Yandún et al. (2015) argue that partitioning based on spectral peaks is more physically accurate than use of a cutoff frequency. However, this results in energy associated with potentially improper partitions (swell with wave periods <7 s). Improvements to the partitioning are not within the scope of this work.

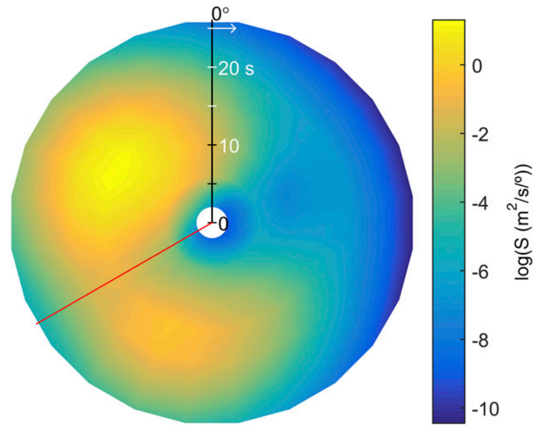

FIG. 3. This method of defining the optimal predictor requires a priori knowledge of the wave climate at the location. The mean directional wave spectrum from 1979 to 2009 for a location offshore of Southern California exhibits bimodality. Evidence for both North and South Pacific swell wave families is present in the secondary peak of the directional wave spectrum. The red line indicates the division of wave energy at 240° between the North and South Pacific swell wave families.

4. Spatiotemporal definition of the predictor

Statistical downscaling efforts link a multivariate predictor to a multivariate predictand through a function that assumes stationarity of patterns and relationships in time. Here, atmospheric conditions were related to deep-water wave parameters. The predictor field was composed of daily standardized SLP anomalies and squared gradients of SLP anomalies (SLPG) at 2° spatial resolution (Wang et al. 2004; Camus et al. 2014a; Perez et al. 2015; Rueda et al. 2016a). Though CFSR SLP fields are available at 0.5° spatial resolution, comparable results and higher computational efficiency without a loss

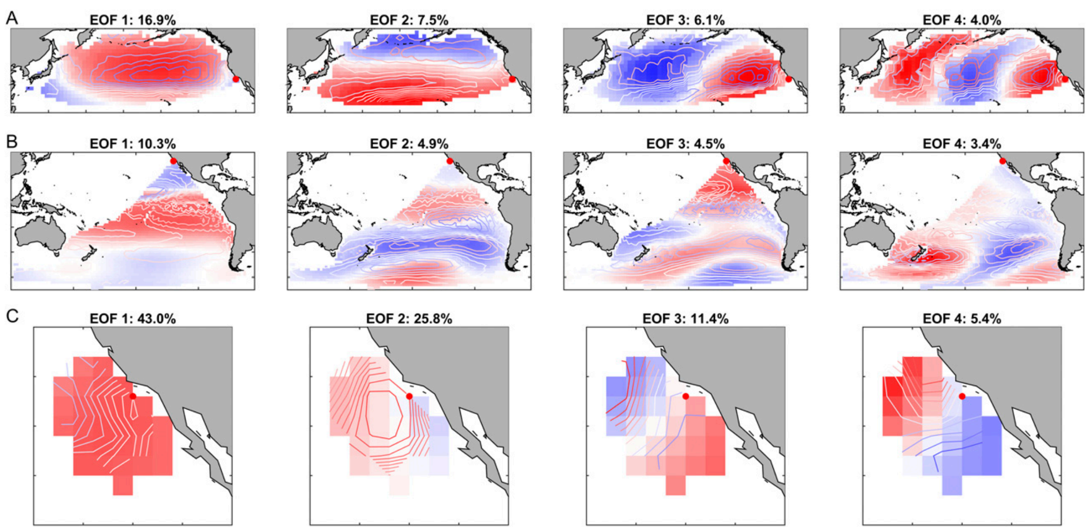

FIG. 4. Empirical orthogonal functions of the (top) NH predictor, (middle) SH predictor, and (bottom) SEA predictor for the location offshore of Southern California (red dot). The SLP anomalies are represented by the shading. Positive anomalies are red and negative anomalies are blue. The anomalies of the squared SLP gradients are represented by the contour lines.

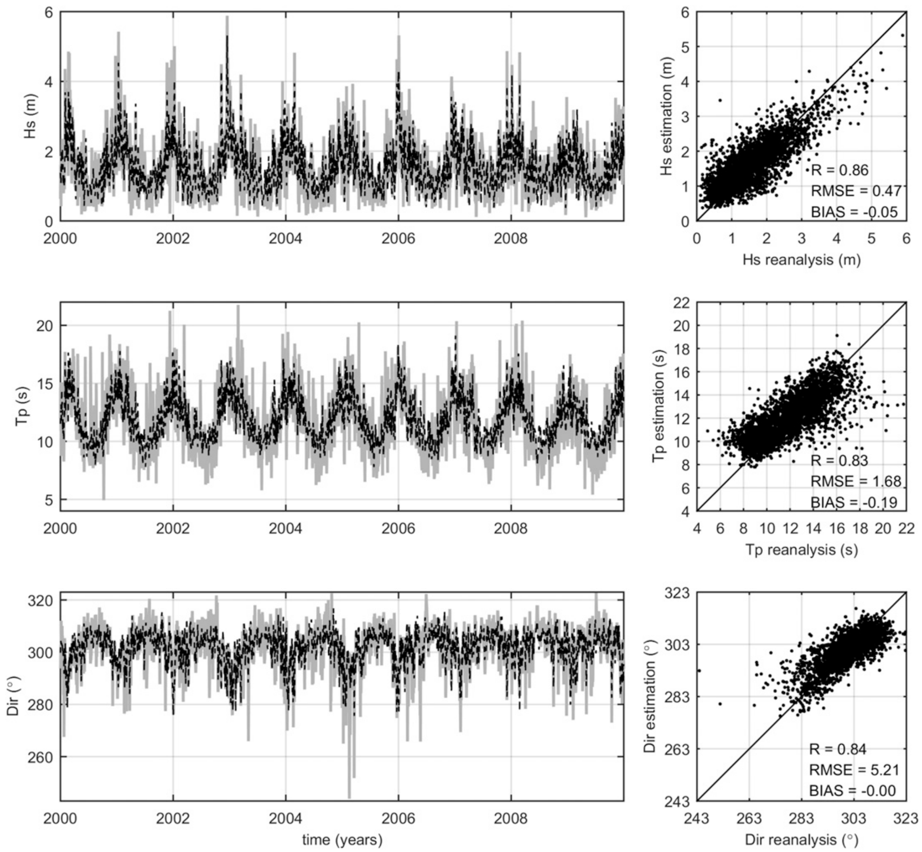

FIG. 5. Multiple multivariate regressions for the location offshore of Southern California of NH significant wave height H_s, peak wave period T_p, and mean wave direction Dir over a validation period (2000–09), where reanalysis parameters are gray and estimated parameters are black. Scatterplots and error statistics are shown for each parameter.

of accuracy were found when upscaling SLP fields to 2° resolution. Similar to the methodology of Camus et al. (2014a), the temporal and spatial parameters of the predictor are defined by the ESTELA effective wave energy and travel time maps.

a. *Temporal range of the predictor*

Camus et al. (2014a) assumed that SLP patterns of the last n days contribute to swell waves that reach the location. According to their methodology, the predictor field for waves on day i was the mean SLP and SLPG over the last n days. Stated differently, waves arriving at the location on day i were statistically linked to the mean atmospheric conditions over days i through $(i - n)$. However, as stated above, wave energy arriving on day i could have been generated by atmospheric conditions over the Western North Pacific on day $i - 12$ and/or by atmospheric conditions over the eastern North Pacific on day $i - 3$ (Fig. 2). Following Camus et al. (2014a) and using $n = 5$ for the case of Southern California has the dual effects of averaging out atmospheric conditions associated with storms (cyclogenesis over 3–4 days) and potentially missing the link between atmospheric conditions and wave energy separated in time by several days to weeks.

We attempt to improve upon the temporal definition to account for the vastness of large ocean basins by building a physically meaningful and intuitive predictor. Here, we assemble the predictor for waves arriving at the location on day i as atmospheric conditions over the area within the 1-day isochrone, atmospheric conditions from day $i - 1$ over the area between the 1- and 2-day isochrones, atmospheric conditions from day $i - 2$ over the area between the 2- and 3-day isochrones, and so on (Fig. 2). For the predictor field P_i,

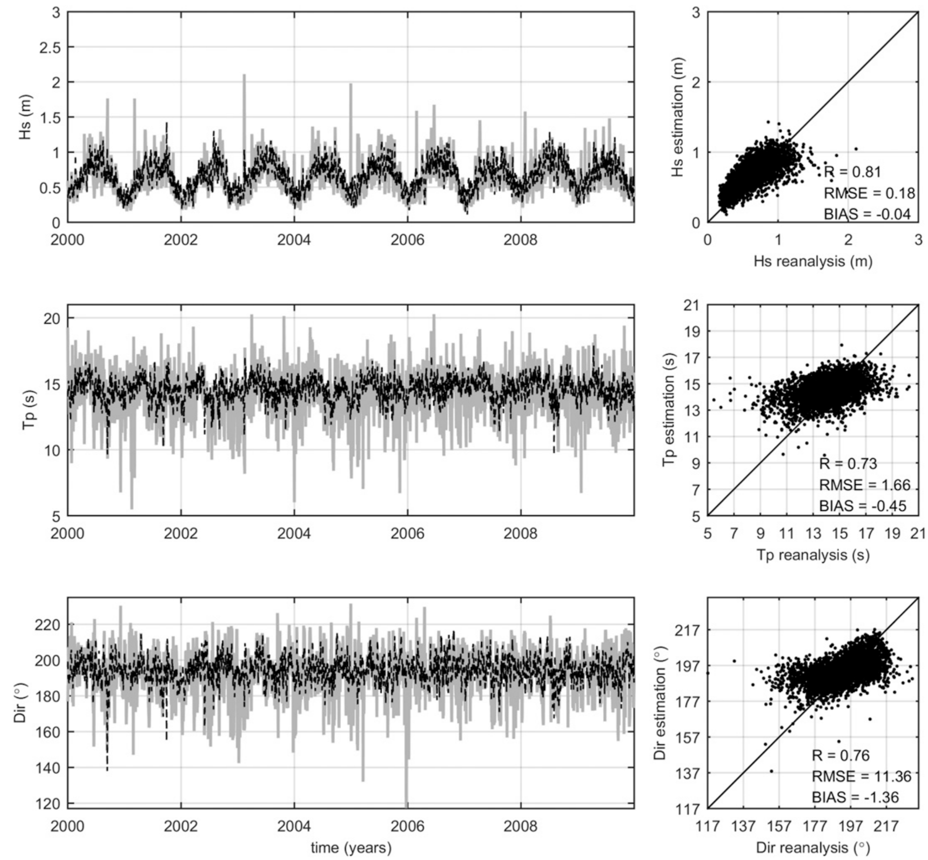

FIG. 6. As in Fig. 5, but for SH.

$$P_i = \{\ldots, \mathrm{SLP}_{i-t+1,\Omega_t}, \mathrm{SLPG}_{i-t+1,\Omega_t}, \ldots\}, \quad \text{and}$$
$$t = \{1, \ldots, T\},$$

where Ω_t is the area between isochrones $t - 1$ and t, and T is the maximum number of isochrones (e.g., 18 days for the North Pacific and 21 days for the South Pacific). Travel times computed with ESTELA are the average travel times for waves generated in a particular region. As such, this temporal delineation of the predictor is subject to uncertainty. However, in ocean basins as large as the Pacific, our improvement of the predictor is substantial.

b. Wave families

For locations experiencing multimodal wave climate, it is important to split both the wave climate and predictor into components defined by wave families. In this work, complexity is added to unimodal bulk wave parameters by accounting for multimodal spectra through redistribution of wave energy from spectral partitions (H_{s0}, T_{p0}, D_{m0}, H_{s1}, T_{p1}, D_{m1}, H_{s2}, T_{p2}, D_{m2}) into wave families. Based on a priori knowledge of the wave climate at the location (Fig. 3), wave energy is redistributed into local seas (SEA), swell generated in the Northern Hemisphere (NH), and swell generated in the Southern Hemisphere (SH):

$$S(f,\theta) = S_{\mathrm{SEA}}(f,\theta) + S_{\mathrm{NH}}(f,\theta) + S_{\mathrm{SH}}(f,\theta),$$

where $S(f, \theta)$ is the full directional spectrum, with f as the frequency and θ as the direction. Wave information for each family (SEA, NH, and SH) was restricted to three commonly used descriptive statistics: H_s, T_p, and D_m (e.g., H_s^{NH}). Wave energy in the zeroth partition was local seas. Wave energy in the first and second partitions was split between Northern and Southern Hemisphere swell using D_m (Fig. 3) and wave generation regions defined with ESTELA (Fig. 2).

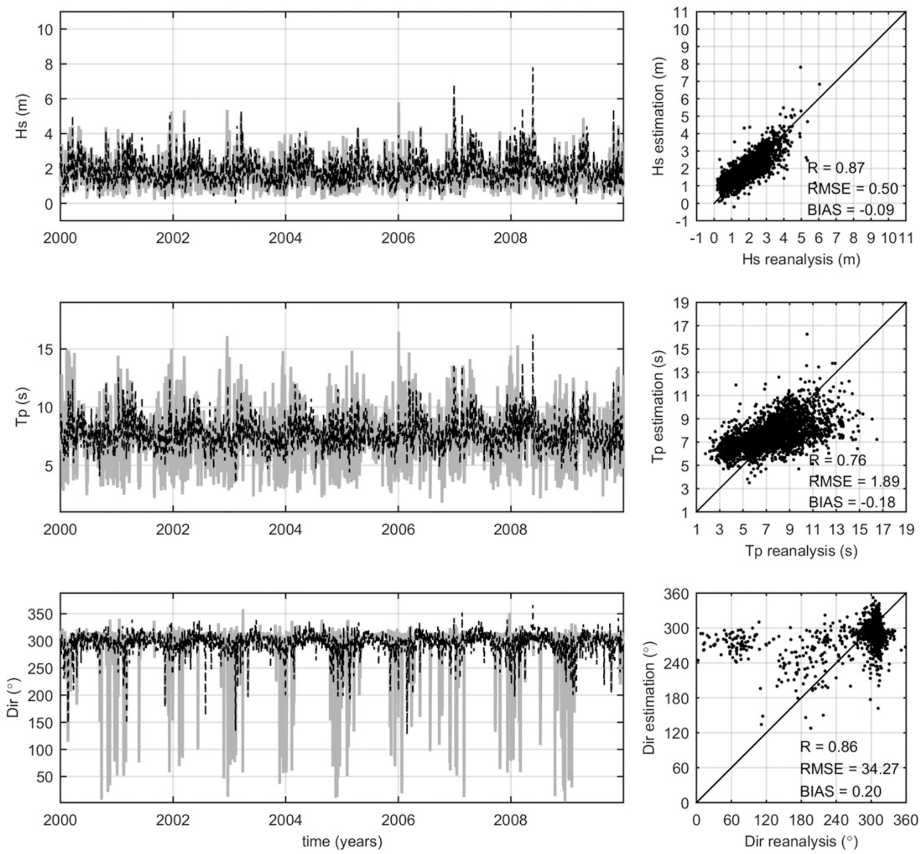

FIG. 7. As in Fig. 5, but for SEA.

We associated the wave generation area in the North Pacific with NH swell and the area in the South Pacific with SH swell (Fig. 2). Mean wave directions approaching from angles between 240° and 360° were considered approaching from the Northern Hemisphere. Mean wave directions approaching from angles between 140° and 240° were considered approaching from the Southern Hemisphere. Though wave family parameters are available hourly, daily means are calculated for this statistical downscaling method.

Substantial improvements could be made to more accurately define seas and different swells. We suspect inconsistencies exist due to both the partitioning algorithm and the lack of T_p as a criterion for identifying either NH or SH.

c. Construction of the predictor

A predictor was defined for each wave family (SEA, NH, and SH). The generation region for SEA encompassed the area over which wave energy reaches the location in 1 day (Fig. 2). The 2- and 3-day generation regions were also tested, with comparable results. To identify generation regions for swell wave families, a threshold was placed on the ESTELA effective wave energy maps, limiting generation regions to areas where energy flux $>2\,\mathrm{kW\,m^{-1}\,{}^{\circ -1}}$ (Fig. 2). The generation region for NH encompassed the area defined in the ESTELA map in the North Pacific (Fig. 2). The generation region for SH encompassed the area defined in the ESTELA map in the South Pacific (Fig. 2). This division coincided nicely with the previous choice to split NH and SH swell at an incident wave direction of 240° (Fig. 2). SLP and SLPG over these identified areas were compiled using isochrones to incorporate the improvements to the temporal definition of the predictor.

5. Multiple multivariate linear regression

At this point in the methodology, we have defined a predictor (P_{NH}, P_{SH}, and P_{SEA}) and predictand (H_s^{NH}, T_p^{NH}, D_m^{NH}, H_s^{SH}, T_p^{SH}, D_m^{SH}, H_s^{SEA}, T_p^{SEA}, and

TABLE 1. Correlation coefficient R, RMSE, and bias for wave parameters significant wave height H_s, peak wave period T_p, and mean wave direction D_m for Southern California and Trujillo, Peru, using the methodology defined in Camus et al. (2014a, C2014 below) and the two improvements of this work: 1) inclusion of isochrones and 2) definition of wave families. In the case of C2014, error statistics are calculated for H_s. In the case of the isochrones improvement, error statistics are calculated for aggregated H_s, T_p, and D_m. In the case of the isochrone and wave family improvement, error statistics are calculated for H_s, T_p, and D_m for each wave family (NH, SH, and SEA).

	Southern California (NH, SH, and SEA)						
	Isochrone				Isochrone + wave family		
	C2014 H_s	H_s	T_p	D_m	H_s	T_p	D_m
R	0.80	0.90	0.76	0.98	(0.86, 0.81, 0.87)	(0.83, 0.73, 0.76)	(0.84, 0.76, 0.86)
RMSE	0.55 m	0.35 m	2.5 s	14°	(0.47, 0.18, 0.50 m)	(1.7, 1.7, 1.9 s)	(5°, 11°, 34°)
BIAS	−0.10 m	−0.07 m	−0.4 s	0°	(−0.05, −0.04, −0.09 m)	(−0.2, −0.5, −0.2 s)	(−0°, −1°, 0°)
	Trujillo, Peru (NH, SH, and SEA)						
	Isochrone				Isochrone + wave family		
	C2014 H_s	H_s	T_p	D_m	H_s	T_p	D_m
R	0.80	0.86	0.75	1.00	(0.84, 0.83, 0.84)	(0.76, 0.78, 0.74)	(0.78, 0.83, 0.70)
RMSE	0.37 m	0.23 m	1.6 s	6°	(0.10, 0.27, 0.24 m)	(1.8, 1.3 1.9 s)	(11°, 8°, 5°)
BIAS	0.04 m	−0.09 m	−0.4 s	0°	(−0.01, −0.08, −0.04 m)	(0.0, −0.3, −0.0 s)	(−1°, −2°, −1°)

D_m^{SEA}) for each wave family. To define a functional relationship between each wave family's multivariate predictor and multivariate predictand, principle component (PC) analysis is first performed on the predictor to reduce the number of dimensions of the problem. We preserve the minimum number of PCs that explain 95% of variance of each wave family. The first four empirical orthogonal functions (EOFs) of the predictors for each wave family are displayed in Fig. 4. The first EOF of the NH predictor describes variation within the strength of the Aleutian low, while the remaining EOFs describe dipolar and tripolar variation over the North Pacific (Trenberth and Paolino 1981). These EOFs are likely correlated to large-scale atmospheric patterns or teleconnections, such as El Niño–Southern Oscillation, Pacific decadal oscillation, or the Pacific–North American pattern, though those correlations were not investigated in this study.

For a statistical downscaling of local wave climate, the predictor in this new PC space can be classified using a K-means algorithm to nonlinearly relate atmospheric and wave conditions for SEA, NH, or SH using a weather-type approach (Camus et al. 2014b). This work only focuses on improvements to the definition of the predictor, but applications of a weather-type approach can be found in Camus et al. (2014b), Perez et al. (2015), Rueda et al. (2016a), and Rueda et al. (2017). Here, to assess the ability of the predictor to define daily wave conditions, a multiple, multivariate, linear regression model is applied to the daily PC and wave time series over a calibration period (1979–99). The regression model is assessed over a validation period (2000–10) using the correlation coefficient R, root-mean-square errors (RMSE), and bias:

$$R = \frac{\sum_{i=1}^{N}(x_{\text{mod}} - \overline{x_{\text{mod}}})(x_{\text{obs}} - \overline{x_{\text{obs}}})}{\sigma_{x_{\text{mod}}}\sigma_{x_{\text{obs}}}},$$

$$\text{RMSE} = \sqrt{\frac{\sum_{i=1}^{N}(x_{\text{obs}} - x_{\text{mod}})^2}{N}}, \quad \text{and}$$

$$\text{bias} = \frac{\sum_{i=1}^{N}(x_{\text{obs}} - x_{\text{mod}})}{N},$$

where the subscripts mod and obs refer to parameters x modeled with the linear regression and "observed" parameters from the wave reanalysis, respectively; σ is the standard deviation of x, and N is the number of data points in the time series.

We test improvements to the predictor in two stages: 1) inclusion of isochrones to account for energy travel time in large ocean basins and 2) splitting of energy into wave families to more completely represent directional wave spectra. First, we assess the predictor with the improvement of the isochrones for total bulk parameters. Second, we incorporate the wave families and isochrones for the fully improved predictor. A summary of these statistics can be found in Figs. 5–7 and Table 1. The improved predictors are successful for reproducing H_s (R = 0.86, 0.81, and 0.87 for NH, SH, and SEA, respectively) and reasonably successful for T_p and D_m ($R \leq 0.7$); T_p is the most difficult parameter to reproduce, likely due to the limited skill of the partitioning algorithm to split local seas and swells in complex sea states. Particularly, the variance is reduced in modeled T_p, meaning the regression is unable to reproduce

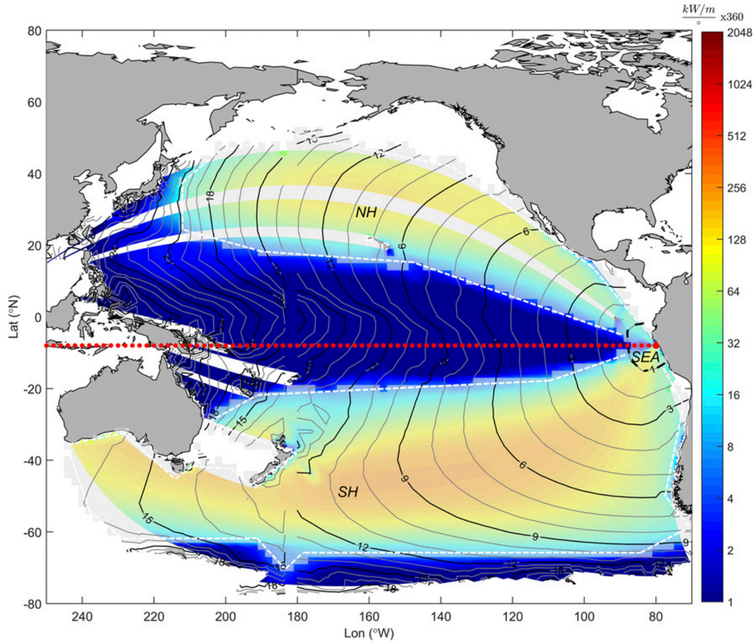

FIG. 8. ESTELA effective wave energy flux (color bar) for the location (large red dot) offshore of Trujillo, Peru. The gray shading over the ocean, outlined generally in white dashed lines, denotes a threshold of 2 kW m^{-1} °$^{-1}$, imposed to define important wave generation regions. The isochrones of travel time are gray and black lines, with every third isochrone labeled in days. The red dotted line emanating from the location shows the demarcation of 270° for North and South Pacific swell families. The shaded area above the red dotted line is the spatial definition of NH. The shaded area below the red dotted line is the spatial definition of SH. The shaded area inside of the 1-day isochrone (black dashed line) is the SEA.

extreme events. RMSE in D_m are quite large for SEA, which can be attributed to the broad range of directions (really 0°–360°) from which local seas can approach the location. Comparing these results to those using the methodology employed in Camus et al. (2014a) shows significant improvement for regions experiencing multimodal wave climates. Camus et al. (2014a) modeled daily and monthly aggregated H_s for the point of interest offshore of Southern California by defining the predictor as SLP and SLPG over the entire Pacific basin (2° resolution) and using $n = 5$ days over which to average atmospheric conditions. Here, comparison of statistics for reproducing daily H_s shows that the amended predictor increases R and decreases RMSE and bias for each wave family (Table 1).

6. Additional application

To further test the new model, the methodology is applied to a location in deep water offshore of Trujillo, Peru (8°S, 79.5°W). Trujillo experiences bimodal wave conditions, with wave energy contributions from both the North and South Pacific, making it an ideal location for the application of this new methodology (Fig. 8). Similar to the application for Southern California, wave energy was split into three distinct wave families. SEA was identified as the first partition. Northern Hemisphere swell and Southern Hemisphere swell were distinguished by D_m. Mean wave directions approaching from angles greater than 270° were considered approaching from the Northern Hemisphere (Fig. 8). Mean wave directions approaching from angles less than 270° were considered approaching from the Southern Hemisphere (Fig. 8). A predictor was defined for each wave family using ESTELA and the methodology described above.

While the methodology is unable to produce correlation coefficients as high as for the Southern California application, it is successful by RMSE and bias metrics (Table 1). Similar to the previous application, the predictors most successfully reproduce H_s (R = 0.84, 0.83, and 0.84 for NH, SH, and SEA, respectively). RMSE and bias are small for H_s, T_p, and D_m. We compare these results again to those employed in Camus et al. (2014a) because this location was included in their original study. Camus et al. (2014a) defined the predictor as the full extent of the Pacific basin using $n = 12$ days. As in the previous application, the improved predictor defined here increases R and decreases RMSE and bias for each wave family (Table 1).

7. Conclusions

An improved method for defining the optimal predictor for statistical downscaling of the multimodal wave climate was presented in the context of two applications where this method yields better results than previous work. In areas where wave spectra exhibit multiple modes due to seas and swells approaching from different generation regions, using a predictor that spatially encompasses only the generation region of the dominant swell mode or describing the wave climate as bulk wave parameters (H_s, T_p, and D_m) of the dominant peak of the spectrum is insufficient. Additionally, in large ocean basins where simultaneously arriving waves may have been generated several days apart, averaging atmospheric conditions across multiday time scales leads to errors in the timing of relationships between the predictor and predictand. By redistributing energy from spectral partitions into wave families and accounting for the average travel time of waves generated in different parts of the basin through isochrones, a unique spatiotemporal predictor can be defined to successfully reproduce local multimodal wave conditions.

The improved predictor is tested for locations offshore of Southern California and Trujillo, Peru. Both locations experience multimodal wave spectra, with energy contributions from local seas and swells generated in both the Northern and Southern Hemispheres. For these applications, the methodology is successful, increasing the ability of the atmospheric conditions to reproduce daily multivariate wave parameters compared to previous work.

Coastal scientists and engineers are moving toward representing wave conditions using the full wave spectrum, as parameterizing the dominant peak of the wave spectrum leads to loss of sea and secondary swell energy. The proposed method is the base of statistical downscaling of local wave climate by weather types, which can be used to project historical and future wave climatologies, simulate realizations of time series of wave parameters, project extremes in wave heights or wave run-up, or project historical and future coastal response. Applications of this methodology are as varied as climate change, coastal flooding hazards, and shoreline change.

Acknowledgments. This work was supported by the U.S. Geological Survey Grant/Cooperative Agreement G15AC00426. AR, JAAA, and FJM were supported by the Spanish Ministerio de Economia y Competitividad Grant BIA2014-59643-R. PC was supported by the Spanish Ministerio de Economia y Competitividad Grant BIA2015-70644-R. JAAA was funded by the Spanish Ministerio de Educación, Cultura y Deporte FPU (Formación del Profesorado Universitario) studentship BOE-A-2013-12235. Support was provided from the U.S. DOD Strategic Environmental Research and Development Program (SERDP Project RC-2644) through the NOAA National Centers for Environmental Information (NCEI). CFSR atmospheric data are available online (at https://climatedataguide.ucar.edu/climate-data/climate-forecast-system-reanalysis-cfsr). Reanalyses of ocean data are available for research purposes through IH Cantabria (contact ihdata@ihcantabria.com).

REFERENCES

Adams, P. N., D. L. Inman, and N. E. Graham, 2008: Southern California deep-water wave climate: Characterization and application to coastal processes. *J. Coastal Res.*, **24**, 1022–1035, doi:10.2112/07-0831.1.

Amante, C., and B. Eakins, 2009: ETOPO1 1 arc-minute global relief model: Procedures, data sources and analysis. NOAA Tech. Memo. NESDIS NGDC-24, 25 pp. [Available online at https://www.ngdc.noaa.gov/mgg/global/relief/ETOPO1/docs/ETOPO1.pdf.]

Antolinez, J. A. A., F. J. Méndez, P. Camus, S. Vitousek, E. M. Gonzalez, P. Ruggiero, and P. Barnard, 2016: A multiscale climate emulator for long-term morphodynamics (MUSCLE-morpho). *J. Geophys. Res. Oceans*, **121**, 775–791, doi:10.1002/2015JC011107.

Camus, P., F. J. Méndez, I. J. Losada, M. Menéndez, A. Espejo, J. Perez, A. Rueda, and Y. Guanche, 2014a: A method for finding the optimal predictor indices for local wave climate conditions. *Ocean Dyn.*, **64**, 1025–1038, doi:10.1007/s10236-014-0737-2.

——, and Coauthors, 2014b: A weather-type statistical downscaling framework for ocean wave climate. *J. Geophys. Res. Oceans*, **119**, 7389–7405, doi:10.1002/2014JC010141.

Crosby, S. C., W. C. O'Reilly, and R. T. Guza, 2016: Modeling long period swell in southern California: Practical boundary conditions from buoy observations and global wave model predictions. *J. Atmos. Oceanic Technol.*, **33**, 1673–1690, doi:10.1175/JTECH-D-16-0038.1.

Erikson, L. H., C. A. Hegermiller, P. L. Barnard, P. Ruggiero, and M. van Ormondt, 2015: Projected wave conditions in the eastern North Pacific under the influence of two CMIP5 climate scenarios. *Ocean Modell.*, **96**, 171–185, doi:10.1016/j.ocemod.2015.07.004.

Espejo, A., P. Camus, I. J. Losada, and F. J. Méndez, 2014: Spectral ocean wave climate variability based on atmospheric circulation patterns. *J. Phys. Oceanogr.*, **44**, 2139–2152, doi:10.1175/JPO-D-13-0276.1.

Graham, N. E., D. R. Cayan, P. D. Bromirski, and R. E. Flick, 2013: Multi-model projections of twenty-first century North Pacific winter wave climate under the IPCC A2 scenario. *Climate Dyn.*, **40**, 1335–1360, doi:10.1007/s00382-012-1435-8.

Hanson, J. L., and R. E. Jensen, 2004: Wave system diagnostics for numerical wave models. *Eighth Int. Workshop on Wave Hindcasting and Forecasting*, JCOMM Tech. Rep. 29, WMO/TD 1319, North Shore, Oahu, Hawaii, U.S. Army Engineer Research and Development Center's Coastal and Hydraulics Laboratory, E3. [Available online at http://www.waveworkshop.org/8thWaves/Papers/E3.pdf.]

Laugel, A., M. Menéndez, M. Benoit, G. Mattarolo, and F. Méndez, 2014: Wave climate projections along the French coastline: Dynamical versus statistical downscaling methods. *Ocean Modell.*, **84**, 35–50, doi:10.1016/j.ocemod.2014.09.002.

Perez, J., M. Menéndez, F. J. Méndez, and I. J. Losada, 2014: ESTELA: A method for evaluating the source and travel time of the wave energy reaching a local area. *Ocean Dyn.*, **64**, 1181–1191, doi:10.1007/s10236-014-0740-7.

——, ——, P. Camus, F. J. Méndez, and I. J. Losada, 2015: Statistical multi-model climate projections of surface ocean waves in Europe. *Ocean Modell.*, **96**, 161–170, doi:10.1016/j.ocemod.2015.06.001.

Portilla-Yandún, J., L. Cavaleri, and G. Ph. Van Vledder, 2015: Wave spectra partitioning and long term statistical distribution. *Ocean Modell.*, **96**, 148–160, doi:10.1016/j.ocemod.2015.06.008.

Rueda, A., P. Camus, F. J. Méndez, A. Tomás, and A. Luceño, 2016a: An extreme value model for maximum wave heights based on weather types. *J. Geophys. Res. Oceans*, **121**, 1262–1273, doi:10.1002/2015JC010952.

——, ——, A. Tomás, S. Vitousek, and F. J. Méndez, 2016b: A multivariate extreme wave and storm surge climate emulator based on weather patterns. *Ocean Modell.*, **104**, 242–251, doi:10.1016/j.ocemod.2016.06.008.

——, and Coauthors, 2017: Multiscale climate emulator of multimodal wave spectra: MUSCLE-spectra. *J. Geophys. Res. Oceans*, doi:10.1002/2016JC011957, in press.

Saha, S., S. Moorthi, H.-L. Pan, X. Wu, J. Wang, and S. Nadiga, 2010: The NCEP Climate Forecast System Reanalysis. *Bull. Amer. Meteor. Soc.*, **91**, 1015–1057, doi:10.1175/2010BAMS3001.1.

Semedo, A., K. Suselj, A. Rutgersson, and A. Sterl, 2011: A global view on the wind sea and swell climate and variability from ERA-40. *J. Climate*, **24**, 1461–1479, doi:10.1175/2010JCLI3718.1.

Snodgrass, F. E., G. W. Groves, K. F. Hasselmann, G. R. Miller, W. H. Munk, and W. H. Powers, 1966: Propagation of ocean swell across the Pacific. *Philos. Trans. Roy. Soc. London*, **A259**, 431–497, doi:10.1098/rsta.1966.0022.

Tolman, H. L., 2009: User manual and system documentation of WAVEWATCH III, version 3.14. U.S. Dept. of Commerce, NOAA, NWS, NCEP Tech. Note, 220 pp. [Available online at http://polar.ncep.noaa.gov/mmab/papers/tn276/MMAB_276.pdf.]

Trenberth, K. E., and D. A. Paolino Jr., 1981: Characteristic patterns of variability in sea level pressure in the Northern Hemisphere. *Mon. Wea. Rev.*, **109**, 1169–1189, doi:10.1175/1520-0493(1981)109<1169:CPOVOS>2.0.CO;2.

Wang, X. L., F. W. Zwiers, and V. R. Swail, 2004: North Atlantic Ocean wave climate change scenarios for the twenty-first century. *J. Climate*, **17**, 2368–2383, doi:10.1175/1520-0442(2004)017<2368:NAOWCC>2.0.CO;2.

——, V. R. Swail, and A. Cox, 2010: Dynamical versus statistical downscaling methods for ocean wave heights. *Int. J. Climatol.*, **30**, 317–332, doi:10.1002/joc.1899.

——, Y. Feng, and V. R. Swail, 2012: North Atlantic wave height trends as reconstructed from the 20th century reanalysis. *Geophys. Res. Lett.*, **39**, L18705, doi:10.1029/2012GL053381.

Wessel, P., and W. H. F. Smith, 1996: A global, self-consistent, hierarchical, high-resolution shoreline database. *J. Geophys. Res.*, **101**, 8741–8743, doi:10.1029/96JB00104.

Wingfield, D. K., and C. D. Storlazzi, 2007: Spatial and temporal variability in oceanographic and meteorological forcing along central California and its implications on nearshore processes. *J. Mar. Syst.*, **68**, 457–472, doi:10.1016/j.jmarsys.2007.02.008.

Young, I. R., S. Zieger, and A. V. Babanin, 2011: Global trends in wind speed and wave height. *Science*, **332**, 451–455, doi:10.1126/science.1197219.

CHAPTER THREE
CONTROLS OF MULTIMODAL WAVE CONDITIONS IN A COMPLEX COASTAL SETTING

Controls of multimodal wave conditions in a complex coastal setting

C.A. Hegermiller*[1,2], A. Rueda[3], L.H. Erikson[2], P.L. Barnard[2],

J.A.A. Antolinez[3], F.J. Mendez[3]

[1] Dept of Ocean Sciences, University of California, Santa Cruz, CA, USA
[2] Pacific Coastal and Marine Science Center, United States Geological Survey, Santa Cruz, CA, USA
[3] Dpto Ciencias y Tecnicas del Agua y del Medio Ambiente, Universidad de Cantabria, Santander, Spain

Abstract

Future coastal hazards emerge from the combined effect of sea level rise, changes to wave conditions, and sea level anomalies associated with storms or low-frequency atmosphere-ocean oscillations. Rigorous characterization of wave climate is limited by the availability of spectral wave observations, the computational cost of dynamical simulations, and the ability to link wave-generating atmospheric patterns with coastal conditions. We present a hybrid statistical-dynamical approach to simulating nearshore wave climate in complex coastal settings, demonstrated in the Southern California Bight, where waves arriving from distant, disparate locations are refracted over complex bathymetry and shadowed by offshore islands. Contributions of wave families and large-scale atmospheric drivers to nearshore wave energy flux are analyzed. Results highlight the variability of influences controlling wave conditions along neighboring coastlines. The universal method demonstrated here can be applied to complex coastal settings worldwide, facilitating analysis of the effects of climate change on nearshore wave climate.

1. Introduction

Robust prediction of present and future coastal hazards, including flooding, beach erosion, cliff retreat, and infrastructure damage, is reliant on a comprehensive understanding of the mean and extreme wave climate in combination with other contributions to total water levels, including tides, sea level rise, and nontidal sea level anomalies [e.g., Benumof et al., 2000; Sallenger, 2000; Ruggiero et al., 2001; Stockdon et al., 2006]. To this end, an extensive body of research exists which characterizes historical deep-water and nearshore wave climate around the world [e.g., Pacific Basin: Barnard et al., 2015; Northeast Pacific: Bromirski et al., 2005; Australia: Harley et al., 2010; Mediterranean: Lionello and Sanna, 2005; Southern California: Adams et al., 2008] using a network of wave buoys [National Data Buoy Center, *ndbc.noaa.gov*; Coastal Data Information Program (CDIP), *cdip.ucsc.edu*] and wave reanalyses [Cox and Swail, 2001; Hanson et al., 2009; Chawla et al., 2012; Reguero et al., 2012]. Additionally, significant progress has been made over the past 5 years in predicting future deep-water wave climate using dynamical models and statistical methods on global [e.g., Hemer et al., 2013; Mori et al., 2010; Wang et al., 2014] and regional [e.g., Graham et al., 2013; Erikson et al., 2015; Rueda et al., 2017] scales.

Downscaling of deep-water wave climate to the nearshore is typically accomplished through dynamical simulation of a limited suite of wave parameters, chosen by a prior knowledge [Adams et al., 2011] or statistical methods [Camus et al., 2011]. Such statistical methods allow the inclusion of new variables, such as wind direction and magnitude. Antolinez et al., [in review] combined statistical and dynamical methods [Camus et al., 2011; 2014] to downscale shoreline change from large-scale atmospheric patterns. However, the connection between deep-water wave climate and nearshore wave conditions or coastal change is not easily described in locations experiencing multimodal deep-water wave spectra, which can be further complicated by complex offshore bathymetry. In these locations, it is useful to avoid bulk parameterizations of the full directional wave spectrum in favor of partitioning the spectrum into wave families originating from unique, discrete generation regions. A more complete description of the directional wave spectrum is crucial, as nearshore wave conditions in complex coastal settings respond to slight changes in energy distributions within the wave spectrum. Development of an approach to adequately describe nearshore wave conditions as they relate to distant wave generation and other physical controls is essential since atmospheric patterns continue to evolve with climate change [Hemer et al., 2013].

Southern California presents an opportunity to demonstrate the utility of a new approach for characterizing complex nearshore wave conditions in light of available projections for future deep-water wave climate. The Southern California Bight (SCB) is a focal area of extensive wave research, with field experiments [e.g., Seymour, 1996; Long and Ozkan-Haller, 2005], modeling studies [e.g., O'Reilly and Guza, 1993; Adams et al., 2008; Adams et al., 2011; Crosby et al., 2016; O'Reilly et al., 2016], and lengthy wave buoy records (*cdip.ucsc.edu*) contributing to the collective knowledge of both wave physics generally and wave climate in this location. Swell arriving from both the North and South Pacific and local seas contribute to the multimodal deep-water wave spectra common to Southern California [Adams et al., 2008; Hegermiller et al., 2016a]. Southern California wave climate is strongly modulated by the El Niño-Southern Oscillation [Adams et al., 2008; Barnard et al., 2015]. Wave energy flux (EF) during El Niño winters is on average ~23% larger than normal in the Eastern North Pacific, though particularly strong El Niño events yield EF ~50% larger than normal [Barnard et al., 2015; 2017]. Extreme coastal erosion during these events results from seasonally elevated sea levels, intensified EF, and more southerly wave directions [ibid.].

The SCB, extending from Point Conception to the Mexican Border, experiences complex wave conditions due to multimodal deep-water conditions, wave refraction and shoaling over highly irregular shelf bathymetry, and wave shadowing, reflection, and diffraction by the Channel Islands, shallow shoals, and Point Conception (Figure 1a). Thus, wave transformation through the Bight results in significant alongshore variations in nearshore wave energy over small scales, O(10 km), meaning adjacent coastlines are sensitive to different parts of the deep-water wave spectrum [Emery, 1958; Pawka et al., 1984; O'Reilly and Guza, 1993; Adams et al., 2011; Crosby et al., 2016; Erikson et al., in review]. The complexity of the wave climate in the SCB limits our ability to predict future nearshore wave conditions because it is functionally impossible to identify the original sources of wave energy through exclusive analysis of the highly transformed nearshore wave spectra. Similar limitations exist in other coastal settings experiencing multimodal wave conditions influenced by shelf bathymetry [e.g., Gorman et al., 2003].

A hybrid statistical-dynamical downscaling approach was developed to assess the contributions of wave families to nearshore wave energy flux (EF) and atmospheric controls on variability in EF in complex coastal settings, with application to the SCB. Wave families are identified as partitions of the wave spectrum corresponding to discrete wave generation areas. The approach uses statistical downscaling of atmospheric patterns to deep-water multimodal wave climate offshore of Southern California [Hegermiller et al., 2016a; Rueda et al., 2017]. A lookup table dynamically translates deep-water wave conditions for each wave family to the SCB nearshore. We calculate the contribution of each wave family to mean EF and annual maximum EF. We also analyze the contribution of each wave family to mean EF for representative atmosphere-ocean patterns [Rueda et al., 2017]. Through this analysis, large-scale atmospheric drivers of nearshore wave EF are identified and latitudinal variability in EF is explored, applicable to complex coastal settings worldwide.

2. Statistical climatology

Hegermiller et al. [2016a] developed a methodology for retaining multimodal wave spectral information in statistical downscaling of atmospheric fields to local wave conditions. The method partitions wave spectra into wave families, which are defined by spectral peaks, a wave speed to wind speed ratio, and discrete generation regions, and introduces a time-lag to relate atmospheric conditions to waves arriving at an offshore location several days later. The method has the potential to accelerate analysis of multimodal wave spectra and their atmospheric drivers in large ocean basins, such as the Pacific Ocean. For a deep-water location offshore of Southern California collocated with CDIP 067 (Figure 1a), Hegermiller et al. [2016a] identified three distinct wave families: 1) North Pacific swell (NH) with wave directions greater than 240° and a wave generation region extending from ~20-60°N in the North Pacific basin, 2) South Pacific swell (SH) with wave directions less than 240° and a wave generation region dominated by the area surrounding New Zealand, and 3) local wind seas (SEA) generated within one day of propagation time from Southern California. Atmospheric conditions over the wave generation regions identified are capable of reproducing daily wave conditions for each wave family with good skill for wave height (H_s) and peak wave period (T_p) and acceptable skill for mean wave direction (Dir) [Hegermiller et al., 2016a]. The inclusion of mean wave direction for each wave family, as opposed to bulk mean wave direction for the full spectrum, is crucial in this work to reproduce the complex multimodal conditions of the SCB.

A statistical downscaling approach based on clustering was used to relate historical, daily deep-water wave climate for NH, SH, and SEA and associated atmospheric conditions at CDIP 067 (Figure 1a) [Rueda et al., 2017]. The statistical relationships were generated from 30-year reanalyses of sea level pressure and wave conditions from 1980-2010: the National Centers for Environmental Prediction’s Climate Forecast System Reanalysis (CFSR) [Saha et al., 2010] and a global ocean wave reanalysis (GOW) generated with WaveWatchIII [Tolman et al., 2002] forced by CFSR near-surface winds [Perez et al., 2015], respectively. The relationships between atmospheric sea level pressure fields within discrete generation regions and deep-water wave parameters (H_s, T_p, and Dir) for each wave family were clustered to generate 36 representative atmosphere-ocean patterns (Figure 2a,b) [Camus et al., 2014; Rueda et al., 2017].

Statistical downscaling of deep-water wave families is computationally efficient while more fully describing the directional wave spectrum. Robust characterization of deep-water wave climate is necessary to assess variability of complex nearshore wave conditions. In this work, we use the statistical relationships developed in Hegermiller et al. [2016a] and Rueda et al. [2017] to force the nearshore wave model.

3. Dynamical translation to the nearshore

Historical daily, deep-water wave conditions (H_s, T_p, Dir) for each wave family (NH, SH, SEA) were translated to the SCB nearshore through a lookup table. The lookup table was populated by the Simulating Waves Nearshore model (SWAN) [Booij et al., 1999] forced in stationary mode over a coarse outer grid and a nested, higher-resolution inner grid extending from Point Conception to the Mexican border and ~25 km offshore (Figure 1a). Bathymetry was populated by the 2013 Coastal California TopoBathy Merge Project [NOAA, 2013]. Resolution varies largely with shoreline features, but is ~3 km over the outer grid in the along- and cross-shore directions and ~200 m over the inner grid in both directions. Wave spectra were computed with 10° directional resolution and 25 frequency bands ranging logarithmically from 0.0417 to 1 Hz.

The SWAN model was forced by deep-water wave triplets (H_s, T_p, Dir) applied uniformly in space along the open boundaries. Boundary wave spectra were constructed from integrated wave parameters assuming a JONSWAP frequency spectral formulation and cosine squared directional spreading. Deep-water H_s was varied from 0.25 to 11 m in 0.25 m increments; deep-water T_p was varied from 4 to 25 s in 3 s increments; deep-water Dir was varied from 104 to 360° in 8° increments. H_S and T_p combinations that yield physically impossible waves due to wave steepness limits were excluded from the suite of simulations. Nearshore wave parameters (H_s, T_p, Dir) were output at 4,802 stations spaced ~100 m apart along the 10 m bathymetric contour from Point Conception to the Mexican Border and at four additional locations coincident with CDIP wave buoys. The lookup table provides a relationship between deep-water and nearshore wave conditions with computational efficiency.

Wave modeling in the SCB and other complex coastal settings has well-documented difficulties [Pawka et al., 1984; O'Reilly and Guza, 1993; Rogers et al., 2007], a few of which are discussed briefly here. The model assumption of stationarity is reasonable for this application. The goal of this work is to simulate daily mean nearshore wave conditions, so we are less concerned with the 4-12 hr lag of waves arriving at the coast and the potential inaccuracies in the timing of different seas and swells [Pawka et al., 1984]. Furthermore, we do not include generation of local seas by wind over the domain and, thus, are not concerned with unrealistic wave growth in response to winds. Other difficulties include the resolution of the grid and bathymetry [Rogers et al., 2007]. Validation of the nearshore wave climate suggests that the resolution used here is sufficient (below) [Hegermiller et al., 2016b]. Lastly, both Pawka et al. [1984] and Rogers et al. [2007] comment on the necessity for accurate, multimodal deep-water wave spectra as forcing. The method applied here approximates the multimodal wave spectra with three wave families, which maintains multimodal complexity, but reduces the information.

The lookup table was validated using daily deep-water conditions for each wave family from GOW. In this work, wave EF is explored, which we define as $EF = {H_s}^2 T_p$. We compare modeled and observed wave frequency spectra using root mean square error (RMSE) of variance density (Figure 3). At the deep-water point, collocated with CDIP 067, daily frequency spectra were constructed using H_s and T_p for each wave family from GOW, assuming a JONSWAP spectral formulation with a peak-shape parameter of 3.3 and no smoothing. Frequency spectra for each wave family were summed to reconstruct the full frequency spectrum. Additionally, daily deep-water wave conditions for each wave family were translated to the SCB interior through the lookup table. Daily frequency spectra were constructed in the same way at four output points collocated with intermediate-water CDIP buoys (Figure 1a). Seasonal mean frequency spectra were compared to observed frequency spectra over

2000-2015 to avoid variability in buoy observations due to hardware and software modifications prior to 2000 [Gemmrich et al., 2011].

At the deep-water point (CDIP 067), monthly mean frequency spectra are well reproduced, with a maximum RMSE of 11.2% of the maximum variance density during summer (JJA; Figure 3). RMSE during other seasons is < 6% of the maximum variance density. The methodology's ability to reproduce wave frequency spectra inside the SCB varies spatially, with the model generally performing better (smaller RMSE) towards the southern extent (Figure 3). RMSE is 36% of the maximum variance density during winter (DJF) at CDIP 028 (central) and exceeds 15% during most seasons at CDIP 107 (northern) and CDIP 028. At CDIP 045 and CDIP 093 in the southern extent of the domain, RMSE is < 15% of the maximum variance density during all seasons.

Large RMSE likely originates from two sources of error. First, variance density of the higher frequency peak during MAM and JJA is underestimated in the model because the dynamical translation to the nearshore through the lookup table does not include wind-wave generation over the SCB. Second, the trimodal nature of modeled spectra suggests a strong bathymetric control (Figure 3). It is possible that large RMSE is related to the resolution of the bathymetry and Channel Islands or the directional resolution, allowing energy to propagate to the nearshore that would otherwise be blocked by the islands or refracted elsewhere by the bathymetry or, on the contrary, blocking energy that should propagate through the islands. Despite these errors, the model successfully captures the shape of the frequency spectra in the SCB, the magnitude and spatial variability of energy in the SCB, and the transition to bimodal spectra during summer months.

4. Results: relative contributions to nearshore energy flux

Daily deep-water wave parameters for North Pacific swell (NH), South Pacific swell (SH), and local seas (SEA) of the statistical climatology [Rueda et al., 2017] were transformed to the SCB nearshore using the lookup table. The contribution of each of these wave families to nearshore wave EF was assessed in two ways: 1) contribution to mean EF and annual maximum EF and 2) contribution by weather types to mean EF.

Daily EF was calculated at each nearshore station as the combined EF delivered by each wave family. Relative contribution of each wave family was calculated as a percentage of daily total EF. Means were calculated over the entire 30-year historical period. Mean EF and contributions of each family to mean EF vary sizably over the domain (Figure 1b,c). Mean EF is largest at the northern and southern boundaries of the SCB, which are both directly exposed to deep-water waves at the tip of Point Conception and San Diego, respectively. Generally, SH mean EF is larger in the southern extent of the domain, with a large shadow in the northern extent from Santa Rosa and Santa Cruz Islands. There are also localized SH shadows in the lee of small headlands. Overall, SH contributes > 50% to mean EF along coastlines that experience relatively small EF and < 40% along coastlines with larger mean EF. NH mean EF exhibits narrow windows, as observed by Pawka et al.

[1984], with a shadow in the northern extent of the SCB, due to shadowing by Point Conception. NH contributes between 14 to 51% to mean EF over the domain. The pattern of variability in SEA mean EF mimics that of NH, though the magnitude is roughly half. SEA contributes at most 42% to mean EF.

Erikson et al. [in review] found that nearshore maximum energy events in the SCB vary in space and do not necessarily coincide with deep-water extreme events. Therefore, we identified annual maxima as the maximum total EF event per wave year (June-June) per nearshore station, allowing the maximum EF event to differ between Santa Barbara and San Diego, for example. Note that the mean EF varies by station per our calculation as well. We calculated the relative contribution of NH, SH, and SEA to annual maximum EF events as a percentage of the annual maximum total EF. The spatial pattern of total mean EF and total annual maximum EF are similar, confirming that refraction and island shadowing strongly control the distribution of energy in the SCB (Figure 1b,d). However, the magnitude and spatial pattern of the contribution of each wave family to annual maximum EF differs greatly from the contribution of each wave family to mean EF (Figure 1c,e). NH dominates annual maximum EF, contributing > 50% over most of the SCB. SH contribution varies largely, from less than 5% to as much as 65% in some locations. Locations where SH contributes > 10% to annual maximum EF are particularly low total EF coasts (Figure 1d,e). SEA annual maximum EF is relatively constant over the domain (Figure 1d), though the contribution of SEA to annual maximum EF varies between 25-65% (Figure 1e).

Large-scale atmospheric patterns also exert control on nearshore EF. We calculated the contribution of NH, SH, and SEA to nearshore EF for each statistical atmosphere-ocean pattern (Figure 2c). Though there is spatial variability associated with refraction and island shadowing, the contribution of each wave family to EF varies largely by pattern. Patterns that dominate boreal winter (DJF) exhibit strong low pressure systems over the North Pacific and large swell waves approaching Southern California from the North Pacific, consistent with expectations for the Aleutian Low and extra-tropical storms to generate waves approaching from westerly and northwesterly directions (Figure 2) [Rueda et al., 2017). For these patterns, which occupy the middle and bottom left of Figure 2c, NH contributes > 70% to mean EF. On the contrary, patterns that dominate boreal summer (JJA) exhibit broad high pressure systems over the North Pacific and California, intense low pressure systems surrounding Antarctica, swell approaching from the South Pacific, and local seas (Figure 2) [Rueda et al., 2017]. These patterns, which occupy the bottom right of Figure 2c, generate wave conditions where SH contributes 60% or more to mean EF. There are no patterns associated with mean EF overwhelmingly dominated by SEA, as there is always a swell component to the SCB wave climate. However, some patterns are associated with local seas that contribute up to 40% to mean EF (Figure 2). It is important to note that the total amount of energy associated with each of these patterns varies.

5. Discussion

Geographic parameters, primarily coastline orientation, shelf bathymetry, and offshore islands, cause spatial variability in nearshore EF and the contributions of different wave families to nearshore EF. The importance of each wave family to nearshore EF varies for mean conditions and annual maximum conditions. Additionally, large-scale atmospheric patterns control the deep-water wave climate and, thus, also the contribution of each wave family to nearshore EF. Neighboring coastlines are sensitive to different atmospheric patterns and deep-water wave conditions. Though these findings are specific to the SCB, complex coastlines with similar controls on nearshore wave conditions can be found throughout the world.

Throughout most of the SCB nearshore, South Pacific swell contributes > 50% to mean EF, emphasizing extensive island and headland shadowing of North Pacific swell. North Pacific swell contributes through narrow windows where wave energy leaks through the Channel Islands. Along SCB coasts that experience relatively low (high) wave energy, South Pacific (North Pacific) swell dominates nearshore annual maximum EF. On average, local seas contribute 19% to mean EF and 40% to annual maximum EF. Crosby et al. [2016] found that local seas accounted for 40% of the wave energy propagating into the SCB at an offshore location. This work did not include local sea generation within the SCB, but accounted for local sea generation within one day propagation time of the deep-water location. Though most of the SCB is fetch-limited by the Channel Islands, generation of local seas is important for more exposed coasts [Erikson et al., in review]. Climate change-driven changes to temperature gradients between land and ocean might enhance generation of local seas in this area, adjusting nearshore EF.

With evolution of atmospheric systems due to climate change, the relative dominance of wave families to the SCB nearshore is subject to change. Using an ensemble of deep-water wave conditions dynamically downscaled from global climate models, Erikson et al. [2015] projected decreasing H_s, increasing T_p, and changing Dir over the 21st century for the CDIP 067 location. Though that work did not include an analysis of multimodal wave conditions, the results yield insight into how wave families may change into the future. Decreasing H_s is related to a poleward shift in North Pacific extra-tropical storm tracks [Yin, 2005; Graham et al., 2013; Erikson et al., 2015]. More southerly Dir and longer T_p are related to the intensification of Southern Ocean wave generation, a consistent feature in global climate model predictions [Arblaster et al., 2011; Hemer et al., 2013]. In the context of the wave families discussed here, over the next century, a poleward shift in extra-tropical storm tracks will decrease the contribution of North Pacific swell to the SCB. Simultaneously, increased wave generation in the Southern Ocean will yield larger contributions from South Pacific swell. South-facing coastlines, which are currently relatively quiescent and home to harbors and ports, will be most affected by increased wave energy from South Pacific swell.

El Niño-Southern Oscillation (ENSO) variability strongly modulates deep-water wave conditions offshore of Southern California. Some studies suggest increases in the frequency and magnitude of El Niño events with climate change [e.g., Cai et al., 2014], though it remains unclear [e.g., Collins et al., 2010; Stevenson, 2012]. The probability of each statistical atmosphere-ocean pattern was calculated for normal, El Niño, and La Niña conditions using the Multivariate ENSO Index (Figure 2d) [Wolter and Timlin, 1998]. By a weighted mean of the total nearshore EF, El Niño conditions deliver a 10% larger EF than normal conditions on average (not shown). This is smaller than previously reported values [Barnard et al., 2015; 2017], possibly due to the Bight-wide calculation used here. Atmosphere-ocean pattern #6 is the most energetic and only occurs during El Niño conditions (Figure 2d).

Through a hybrid statistical-dynamical methodology, we assessed the geographic controls on, the contributions of multimodal wave conditions to, and the large-scale atmospheric drivers of the spatial variability of nearshore wave energy flux in a complex coastal setting. Wave families dominate different discrete sections of coastline during mean and annual maximum conditions. Additionally, the influence of characteristic atmospheric patterns on nearshore energy flux was explored during average, winter, summer, El Niño, and La Niña conditions. The method demonstrated in this work allows for an elegant characterization of nearshore wave conditions in light of climate change-induced evolution of wave-generating atmospheric patterns. In complex coastal settings, the nearshore wave climate can be highly sensitive to changes in deep-water wave climate, and therefore impacts to neighboring coastlines differ, exposing certain sections to increased coastal hazards in the future.

Acknowledgements

This work was funded by the U.S. Geological Survey (USGS) Coastal and Marine Geology Program. The authors thank Jorge Perez, I.H. Cantabria, for providing the GOW wave hindcast and for assistance with wave spectra, and Sean Vitousek, University of Chicago, for a helpful review. This material is based upon work supported by the U.S. Geological Survey under grant/cooperative agreement GI5AC00426. A.R., J.A.A.A., and F.J.M. acknowledge the support of the Spanish "Ministerio de Economía y Competitividad" under grant BIA2014-59643-R. J.A.A.A. was funded by the Spanish "Ministerio de Educación, Cultura y Deporte" FPU (Formación del Profesorado Universitario) studentship BOE-A-2013-12235.

REFERENCES

Adams, P.N., D.L. Inman, and N.E. Graham, 2008. Southern California deep-water wave climate: characterization and application to coastal processes. *Journal of Coastal Research*, **24**(4): 1022-1035, doi:10.2112/07-0831.1.

Adams, P.N., D.L. Inman, and J.L. Lovering, 2011. Effects of climate change and wave direction of longshore sediment transport patterns in Southern California. *Climactic Change*, **109**(S1), S211-S228.

Arblaster, J. M., G. Meehl, and D.J. Karoly, 2011. Future climate change in the Southern Hemisphere. Competing effects of ozone and greenhouse gases. *Geophysical Research Letters*, **38**, L02701.

Barnard, P.L. and Coauthors, 2015. Coastal vulnerability across the Pacific dominated by El Niño/Southern Oscillation. *Nature Geosciences*, **8**, 801-808, doi:10.1038/NGEO2539.

Barnard, P.L. and Coauthors, 2017. Extreme oceanographic forcing and coastal response due to the 2015-2016 El Niño. *Nature Communications*, **8**, doi:10.1038/ncomms14365.

Benumof, B.T., C.D. Storlazzi, R.J. Seymour, and G.B. Griggs, 2000. The relationship between incident wave energy and seacliff erosion rates: San Diego County, California. *Journal of Coastal Research*, **16**(4), 1162-1178.

Booij, N., R.C. Ris, and L.H. Holthuijsen, 1999. A third-generation wave model for coastal regions. 1. Model description and validation. *Journal of Geophysical Research*, **104**(C4), 7649-7666.

Bromirski, P.D., D.R. Cayan, and R.E. Flick, 2005. Wave spectral energy variability in the northeast Pacific. *Journal of Geophysical Research*, **110**, doi:10.1029/2004JC002398.

Camus, P., F.J. Mendez, and R. Medina, 2011. A hybrid efficient method to downscale wave climate to coastal areas. *Coastal Engineering*, **58**, 851-862, doi:10.1016/j.coastaleng.2011.05.007.

Camus, P., and Coauthors, 2014. A weather-type statistical downscaling framework for ocean wave climate. *Journal of Geophysical Research: Oceans*, **119**, 7389-7405, doi:10.1002/2014JC010141.

Chawla, A., D. Spindler, and H. Tolman, 2012. 30 Year Wave Hindcasts using WAVEWATCH III with CFSR winds: Phase 1. Technical Note.

Collins, M., and Coauthors, 2010. The impact of global warming on the tropical Pacific Ocean and El Niño. *Nature Geosciences*, **3**, 391-397, doi: 10.1038/ngeo868.

Cox, A.T. and V.R. Swail, 2001. A global wave hindcast over the period 1958-1997: Validation and climate assessment. *Journal of Geophysical Research*, **106**, C2, 2313-2329.

Crosby, S.C., W.C. O'Reilly, and R.T. Guza, 2016. Modeling long period swell in southern California: practical boundary conditions from buoy observations and global wave model predictions. *Journal of Atmospheric and Oceanic Technology*, **33**, 1673-1690, doi:10.1175/JTECH-D-16-0038.1.

Emery, K.O., 1958. Wave patterns off Southern California. *Journal of Marine Research*, **17**, 133-140.

Erikson, L.H., C.A. Hegermiller, P.L. Barnard, P. Ruggiero, and M. van Ormondt, 2015. Projected wave conditions in the Eastern North Pacific under the influence of two CMIP5 climate scenarios. *Ocean Modelling*, **96**, 171-185, doi:10.1016/j.ocemod.2015.07.004.

Erikson, L.H. and Coauthors, in review. Selection of storm events for deterministic modeling of extreme coastal flood events in response to climate change.

Gemmrich, J., B. Thomas, and R. Bouchard, 2011. Observational changes and trends in northeast Pacific wave records. *Geophysical Research Letters*, **38**(22), doi: 10.1029/2011GL049518.

Gorman, R.M., K.R. Bryan, and A.K. Laing, 2003. Wave hindcast for the New Zealand region: Nearshore validation and coastal wave climate. *New Zealand Journal of Marine and Freshwater Research*, **37**, 567-588, doi: 10.1080/00288330.2003.9517190.

Graham, N.E., D.R. Cayan, P.D. Bromirski, and R.E. Flick, 2013. Multi-model projections of twenty-first century North Pacific winter wave climate under the IPCC A2 scenario. *Climate Dynamics*, **40**, 1335-1360.

Hanson, J.L., B.A. Tracy, H.L. Tolman, and R.D. Scott, 2009. Pacific Hindcast Performance of Three Numerical Wave Models. *Journal of Atmospheric and Oceanic Technology*, **26**: 1614-1633.

Harley, M. D., I.L. Turner, A.D. Short, and R. Ranasinghe, 2010. Interannual variability and controls of the Sydney wave climate. *International Journal of Climatology*, **30**, 1322-1335.

Hegermiller, C.A. and Coauthors, 2016a. A multimodal wave spectrum-based approach for statistical downscaling of local wave climate. *Journal of Physical Oceanography*, **47**, doi: 10.1175/JPO-D-16-0191.1.

Hegermiller, C.A., L.H. Erikson, and P.L. Barnard, 2016b. Nearshore waves in Southern California: hindcast, and modeled historical and 21st-century projected time series. U.S. Geological Survey summary of methods to accompany data release. doi:10.5066/F7N29V2V.

Hemer, M. A., Y. Fan, N. Mori, A. Semedo, and X.L.Wang, 2013. Projected changes in wave climate from a multi-model ensemble. *Nature Climate Change*, **3**, 471-476.

Lionello, P. and A. Sanna, 2005. Mediterranean wave climate variability and its links with NAO and Indian Monsoon. *Climate Dynamics*, **24**, 611-623.

Long, J.W. and H.T. Ozkan-Haller, 2005. Modeling of the wave and circulation field at the Nearshore Canyon Experiment (NCEX). *Coastal Engineering*, 1417-1428.

Mori, N., T. Yasuda, H. Mase, T. Tom, and Y. Oku, 2010. Projections of extreme wave climate change under global warming. *Hydrologic Research Letters*, **4**, 15-19.

National Oceanic and Atmospheric Administration (NOAA), Department of Commerce (DOC), National Ocean Service (NOS), Office for Coastal Management (OCM), 2014. 2013 NOAA Coastal California TopoBathy Merge Project. https://coast.noaa.gov/dataviewer/#/lidar/search/where:ID=2612.

O'Reilly, W.C. and R.T. Guza, 1993. A comparison of two spectral wave models in the Southern California Bight. *Coastal Engineering*, **19**, 263-282.

O'Reilly, W.C., C.B. Olfe, J. Thomas, R.J. Seymour, and R.T. Guza, 2016. The California coastal wave monitoring and prediction system. *Coastal Engineering*, **116**, 118-132, doi:10.1016/j.coastaleng.2016.06.005.

Pawka, S.S., D.L. Inman, and R.T Guza, 1984. Island sheltering of surface gravity waves: model and experiment. *Continental Shelf Research*, **3**, 35-53.

Reguero, B.G., M. Menéndez, F.J. Méndez, R. Mínguez, and I.J. Losada, 2012. A Global Ocean Wave (GOW) calibrated reanalysis from 1948 onwards. *Coastal Engineering*, **65**, 38-55, doi:10.1016/j.coastaleng.2012.03.003.

Rueda, A., and Coauthors, 2017. Multiscale climate emulator of multimodal wave spectra: MUSCLE-spectra. *Journal of Geophysical Research: Oceans*, doi:10.1002/2016JC011957.

Ruggiero, P., P.D. Komar, W.G. McDougal, J.J. Marra, and R.A. Beach, 2001. Wave runup, extreme water levels and the erosion of properties backing beaches. *Journal of Coastal Research*, **17**(2), 407-419.

Sallenger, A.H., 2000. Storm impact scale for barrier islands. *Journal of Coastal Research*, **16**(3), 890-895.

Seymour, R., 1996. Wave climate variability in Southern California. *Journal of Waterway, Port, Coastal, and Ocean Engineering*, **122**(4), 182-186.

Stevenson, S.L., 2012. Significant changes to ENSO strength and impacts in the twenty-first century: Results from CMIP5. *Geophysical Research Letters*, **39**, doi: 10.1029/2012GL052759.

Stockdon, H.F., R.A. Holman, P.A. Howd, and A.H. Sallenger, 2006. Empirical parameterization of setup, swash, and runup. *Coastal Engineering*, **53**, 573-588, doi:10.1016/j.coastaleng.2005.12.005.

Tolman, H.L. and Coauthors, 2002. Development and implementation of wind generated ocean surface wave models at NCEP. *Weather and Forecasting*, **17**, 311-333.

Wang, X.L., Y. Feng, and V.R. Swail, 2014. Changes in global ocean wave heights as projected using multimodel CMIP5 simulations. *Geophysical Research Letters*, doi:10.1002/2013GL058650.

Yin, J.H., 2005. A consistent poleward shift of the storm tracks in simulations of 21st century climate. *Geophysical Research Letters*, **32**, L18701.

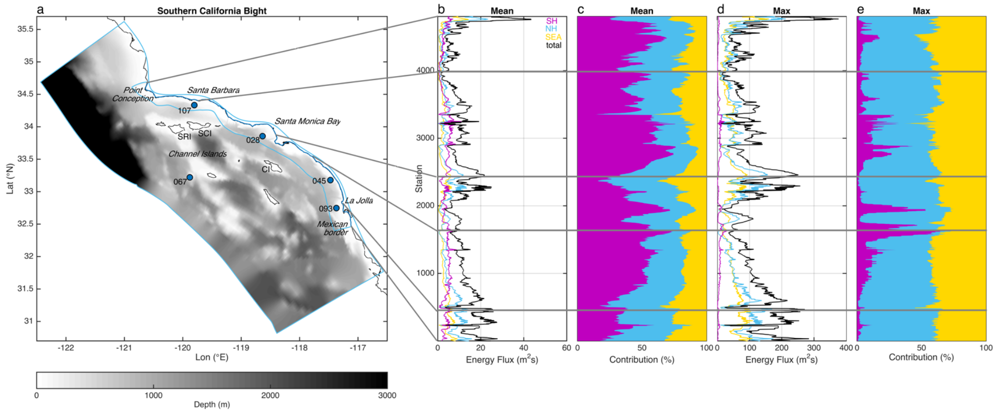

Figure 1. a) The study area is the Southern California Bight nearshore. The Southern California Bight exhibits complex bathymetry, including Santa Rosa Island (SRI), Santa Cruz Island (SCI), and Catalina Island (CI). The blue boxes encompass the outer low-resolution grid and inner high-resolution grid of the SWAN simulations used in the dynamical component. The purple circles indicate CDIP buoys used for validation. Lines emanating from the coastline in (a) towards (b-e) serve to stretch the coastline to the spacing of stations. Station number in (b-e) increases from 1 at the Mexican border to 4802 at Point Conception. b) Total mean energy flux and mean energy flux associated with North Pacific swell (NH), South Pacific swell (SH), and local seas (SEA). c) Contribution, in percent, of each wave family to total mean energy flux. d) Total annual maximum energy flux and annual maximum energy flux associated with each wave family. e) Contribution, in percent, of each wave family to total annual maximum energy flux.

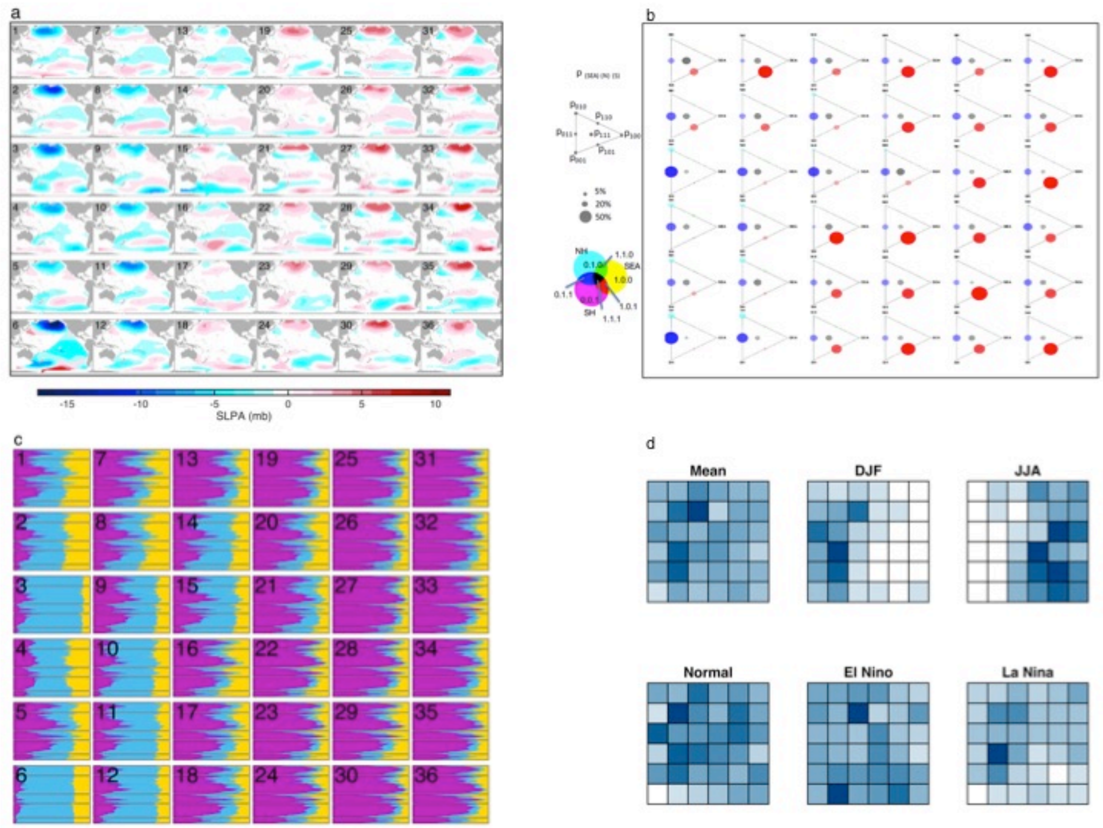

Figure 2. a) Statistical atmosphere-ocean patterns of sea level pressure anomalies that generate wave conditions offshore of Southern California (CDIP 067; Figure 1a). b) For each pattern, the frequency of waves classified as North Pacific swell (NH), South Pacific swell (SH), local wind seas (SEA), or a combination of waves from each family, where color shows which waves are present. Reprinted from Rueda et al. [2017]. c) Contribution, in percent, of each wave family to total mean energy flux per pattern. Axes and colors are the same as in Figure 1c,e. d) The frequency of each pattern for the mean climate, boreal winter (DJF), boreal summer (JJA), normal conditions, El Niño conditions, and La Niña conditions, where darker blue shades indicate more occurrences of that weather type.

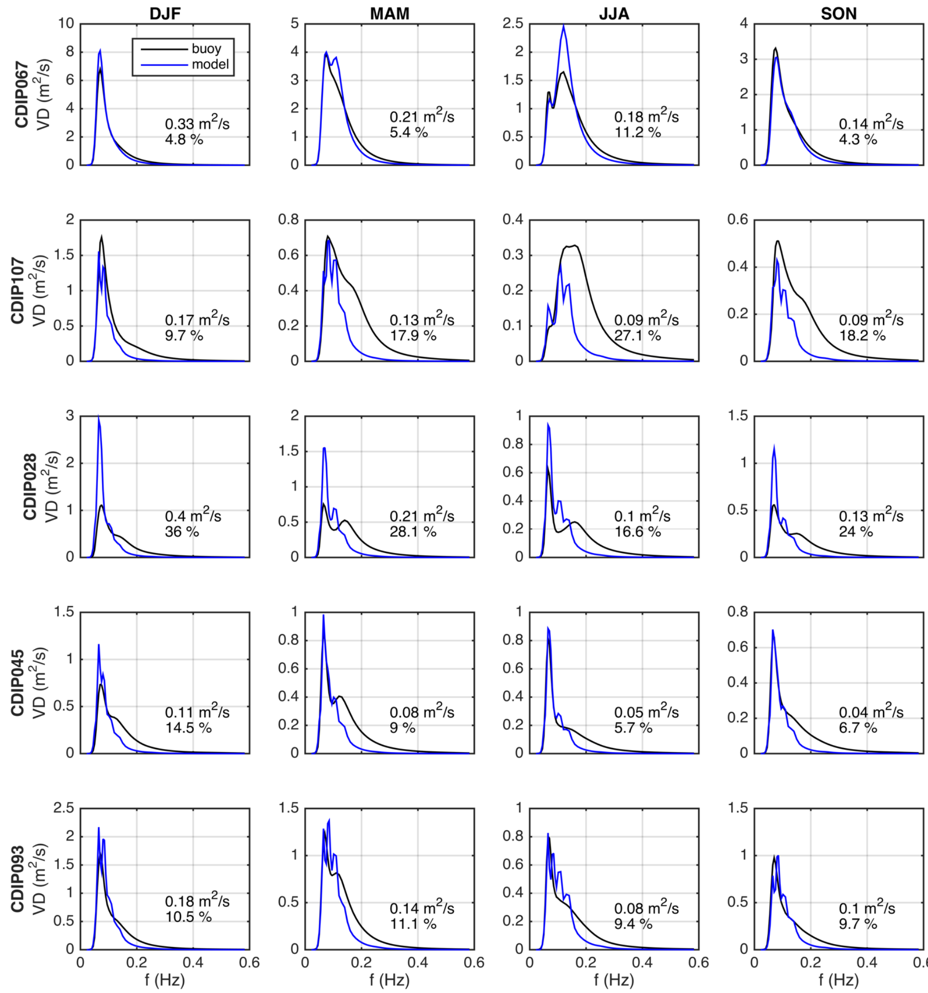

Figure 3. Model and buoy wave frequency spectra by season for five CDIP locations (Figure 1a). Note that the variance density changes for each plot. Root mean square error is expressed in variance density and also as a percentage of the maximum observed variance density for each season and wave buoy.

CHAPTER FOUR
TIDALLY-DRIVEN CIRCULATION OF AN IDEALIZED SMALL, SHALLOW ESTUARINE EMBAYMENT

Tidally-driven circulation of an idealized small, shallow estuarine embayment

Abstract

Small, shallow embayments flanking deep estuarine channels provide critical habitat for estuarine flora and fauna and trap muddy sediments that ultimately provide accretionary material for surrounding marshes. This study investigates the circulation of a shallow (5 m depth) embayment with channelized tidal flow in a nonrotating, long, linear estuary (5 km wide). Model simulations are conducted for idealized, semicircular embayments with radii smaller than the width of the channel. The base run has geometric scales (radius = 1.5 km) similar to Corte Madera Bay, a small, human-altered bay in San Francisco Bay. Simulations are forced with a M_2 barotropic tide and a constant freshwater flux, resulting in steady stratification and a top to bottom salinity difference of ~10. Eddies are observed to form within the embayment on both phases of the tide, though there are distinct asymmetries between ebb and flood. Enhanced across-channel flows across the mouth of the embayment are associated with injection of relatively high-salinity water into the shallow embayment from below the pycnocline in the adjacent channel. Vertical diffusion mixes the salt into the bay surface waters. During slack tides, the eddy is ejected from the embayment, injecting anomalously high salinity waters into the surface of the channel. The across-channel momentum balance across the mouth of the embayment is dominated by the barotropic pressure gradient and across-channel advection, which is a different balance than occurs in the channel away from the embayment. The net

effect of this circulation is elevated bay-averaged salinity compared to the average salinity of the surface 5 m of the adjacent channel. Model results for embayments with smaller and larger radii than the base run, but all smaller than the channel width, display qualitatively similar circulation to the base run, though the magnitude of the salt flux across the mouth of the embayment differs. For the range of radii tested, we find an inverse relationship between embayment radius and salinity of the bay relative to the channel. The magnitude of the barotropic pressure gradient is responsible for the observed relationship. The embayment circulation likely also drives spatial variability in bed and suspended sediments in the estuary.

1. Introduction

Comprehensive understanding of the along-channel and across-channel circulations of varied estuarine environments has received considerable effort over the past 50 years. The along-channel estuarine circulation, an order of magnitude smaller than tidal flow, in which saline waters flow into the estuary at depth and relatively fresh waters exit the estuary at the surface, was described early in the development of the field by Hansen and Rattray (1965). In this seminal paper, Hansen and Rattray (1965) introduced the dominant momentum balance in the along-channel direction between the vertical stress divergence and the baroclinic pressure gradient, set up by along-channel salinity gradients between oceanic and riverine conditions. Recent work has challenged this leading balance and identified nonlinear advective flux divergence, mostly dominated by the across-channel and vertical divergences, as an equally important driver of estuarine circulation in systems with large mixing (Lerczak and Geyer, 2004; Basdurak and Valle-Levinson, 2012). Along-channel advective flux divergence can also be important to the along-channel estuarine circulation in estuaries with significant variations in along-channel bathymetry (Basdurak and Valle-Levinson, 2012).

The across-channel circulation, often an order of magnitude smaller than along-channel flows, is of particular importance for the dispersion of tracers (e.g., sediment, salt, pollutants) throughout estuaries (Smith, 1976; Geyer, 1993). Transport of salt and momentum by the across-channel circulation can also influence the strength and structure of the along-channel estuarine circulation (Lerczak and Geyer, 2004; Cheng et al., 2009; Basdurak and Valle-Levinson, 2012). Across-channel flows are driven primarily by differential advection of along-channel salinity gradients (Nunes and Simpson, 1985), boundary mixing over a sloping bottom (Phillips, 1970; Chen and Sanford, 2009), flow curvature (Rozovski, 1957; Kalkwijk and Booij, 1986; Lacy and Monismith, 2001), and Coriolis forcing.

For primary flow oriented in x in Cartesian coordinates, the across-channel momentum equation is

$$\frac{\partial v}{\partial t} + u\frac{\partial v}{\partial x} + v\frac{\partial v}{\partial y} + w\frac{\partial v}{\partial z} + fu = -g\frac{\partial \eta}{\partial y} - \frac{g}{\rho_0}\frac{\partial}{\partial y}\int \rho \partial z + \frac{\partial}{\partial z}\left(A_v \frac{\partial v}{\partial z}\right)$$

where u, v, and w are the velocity components in x (along-channel), y (across-channel), and z, respectively, f is the Coriolis parameter, g is acceleration due to gravity, ρ is density, ρ_0 is a reference density, η is sea surface height, and A_v is turbulent vertical viscosity. The first term on the left describes the time rate of change of across-channel velocity. The second through fourth terms on the left describe nonlinear advection of across-channel velocity. The last term on the left describes Coriolis forcing. The first and second terms on the right describe forcing by the barotropic and baroclinic pressure gradients, respectively. The last term on the right describes changes to the across-channel velocity by viscous forces. When projecting the flow into curvilinear coordinates where the along-channel direction follows streamlines of depth-averaged flow, the term $-\frac{u_s^2}{R}$ can be added to the left side of the above equation to account for flow curvature. s indicates the streamwise coordinate and R is the radius of curvature of streamlines. In estuaries where differential advection or boundary mixing over a sloping bottom creates across-channel salinity gradients and no Coriolis or flow curvature, the dominant momentum balance in the across-channel direction is between vertical stress divergence and the baroclinic pressure gradient. In cases where flow curvature is locally important, across-channel circulation is driven by a balance between centrifugal accelerations and the barotropic pressure gradient. When Coriolis forcing dominates, across-channel circulation is geostrophic and depends on the phase of the tide.

Development of across-channel flows has been examined for flow in curving channels, around headlands, islands, and shoals, and in straight channels under varying stratification. However, across-channel flows developed in the vicinity of small (dimensions < channel width), shallow embayments flanking estuarine channels have not received much attention. Small, shallow embayments provide critical habitat for estuarine flora and fauna and trap muddy sediments that ultimately provide accretionary material for surrounding marshes (Lacy and Hoover, 2011). An understanding of circulation and mechanisms that control fluxes of sediment, salt, or contaminants into and out of embayments can inform estuarine restoration efforts and mitigation of erosion hazards. Sediment fluxes are of critical importance for marsh accretion in the face of sea level rise and changes to riverine sediment loads under climate change scenarios.

This study investigates channelized tidal flow past a shallow, estuarine embayment and the resulting circulation set up inside the embayment. The base run explores a small, symmetric embayment with a radius that is 30% (1.5 km) the width of the channel (5 km) and a depth that is 25% (5 m) the maximum depth of the channel (20 m). The radius of the embayment is varied in model sensitivity experiments but is kept smaller than the width of the channel. The model configuration is described in the following section. Section 3 describes the structure and dynamics of the channel circulation without the embayment. Section 4 discusses the embayment circulation using quantifications of bulk flux and mixing. An exploration of the dynamics through the momentum balance is included. Lastly, in section 5, results of the model sensitivity experiment are detailed to provide context for the scale of the embayment circulation.

2. Model description

To simulate the dynamics of an idealized estuarine embayment, the full extent of a linear, channelized estuary was modeled using the Regional Ocean Modeling System (ROMS; Haidvogel et al., 2000; Shchepetkin and McWilliams, 2005). ROMS is a three-dimensional, free surface, terrain-following hydrodynamic model that solves the Reynolds-Averaged Navier Stokes equations using a finite differences method assuming hydrostatic equilibrium and Boussinesq appromixations on a curvilinear Arakawa C grid. The model is run with a third-order upstream horizontal advection scheme and a fourth-order centered vertical advection scheme for tracers and momentum. Horizontal viscosity and diffusivity are zero, though numerical viscosity and diffusivity are present. Vertical mixing follows a generic length scale closure specified as k-ε with a Kantha and Clayson (1994) stability function. Background vertical viscosity and diffusivity are 10^{-5} m^2s^{-1} and 10^{-5} m^2s^{-1}, respectively. A quadratic drag law is used to calculate the bottom stress, where the drag coefficient is 0.003. There is no Coriolis forcing.

The model domain consists of an outer grid representing the full estuary and a nested grid representing the central portion of the estuary with the embayment added (Figure 1A). The outer grid is 300 km long and 11 km wide, extending from oceanic conditions at the west end and riverine conditions at the east end. The linear estuary is limited to 5 km in width using land masks on the north and south sides of the domain with no slip conditions, effectively implementing closed boundaries along the estuary edges. Horizontal resolution of the outer grid is 180 m in the x and y directions, where x and y are positive in the eastward and northward directions, respectively.

Vertical resolution varies with the bathymetry using 20 terrain-following s-coordinates. Higher vertical resolution is supplied at the surface and bottom of the water column. At the oceanic end, the bottom depth is constant at 200 m for 25 km then linearly decreases to 20 m over the following 75 km (Figure 1B). Between x = 100 and 200 km, the channel is uniform in x and parabolic in y with a maximum depth of 20 m at the center and 5 m at the sides (Figure 1D). Between x = 200 and 275 km, the depth linearly decreases to 5 m and then is constant for the remaining 25 km of the domain.

The model is forced by a barotropic tide and freshwater flux. A M_2 tide is implemented at the oceanic end through free surface and barotropic velocity variations specified with Chapman and Flather conditions, respectively. Maximum tidal fluxes are 8000 m^3/s. A constant freshwater flux of 1000 m^3/s is implemented at the riverine end through imposition of a barotropic velocity. Radiation boundary conditions are applied at the western edge and clamped boundary conditions are applied at the eastern edge. Incoming oceanic salinity is loosely nudged to 30 over a 3-hour timescale; incoming riverine salinity is 0. The salinity intrusion extends ~270 km into the channel and is not noticeably affected by the clamped eastern boundary condition. The temperature is uniform and constant at 10°C. Turbulent kinetic energy is generated within the domain by the mixing scheme, and a zero gradient condition on this quantity is imposed at the boundaries. The domain is initialized with zero velocities, zero free surface elevation, a linear horizontal gradient in salinity, and no vertical stratification. The outer grid is run for 110 days with a 30 s time step for the baroclinic mode and 1.5 s time step for the barotropic mode. After 100 days, domain-averaged salinity varies over a tidal cycle, but is in steady state over consecutive tidal cycles.

The nested grid is 50 km long and 11 km wide, centered on the midpoint of the outer grid, x = 150 km (Figure 1A). Horizontal resolution is 60 m in both the x and y directions. The nested grid is simulated in a channel-only state, in which the bathymetry in the channel is the same as that of the outer grid, to understand the dynamics of the chosen forcing without added complexity of the embayment. Apart from this channel-only run, in the center of the domain at the northern boundary, an embayment that extends northwards is added. For the base run, the embayment is a semicircle with a radius of 1.5 km and smoothed corners at the junctions between the bay and channel (Figure 1C). Smoothed corners do not qualitatively impact the resulting circulation. The embayment radius of the base run is similar to that of Corte Madera Bay, a small, human-altered embayment in San Francisco Bay which is the subject of current restoration efforts (Lacy and Hoover, 2011). In sensitivity experiments, the embayment radius is altered through the range [0.75:3 km] (Table 1). The depth of the embayment is 5 m, which is equal to the shallow depth of the channel. Shoaling bathymetry within the embayment was tested, but does not qualitatively alter the circulation discussed. Free surface elevation, barotropic and depth-varying velocity, salinity, temperature, and turbulent kinetic energy at the east and west boundaries of the nested grid are extracted from the outer grid every 15 minutes over the final 10 days of the simulation. The boundaries of the nested grid are clamped to these conditions. Initial conditions for the nested grid are interpolated values from the outer grid. The embayment is initialized by imposing the conditions from the channel at the mouth of the embayment horizontally throughout the bay.

Analysis of the tidal and tidally-averaged circulation is performed over the last tidal cycle of the simulation, ~9.5 days after initialization of the nested grid and ~109.5 days after initialization of the outer grid. All analyzed variables presented are 15-minute averages. Tidal hours refer to the nearest model output to 1.035-hour intervals of the M_2 tidal cycle (12.42 hour/12). Nearest model output was < 7.5 minutes from the tidal hour.

3. Channel dynamics

a. Circulation

We begin by describing the channel-only circulation to later illuminate the complex dynamics of the bay. The salinity intrusion extends ~270 km into the estuary (Figure 2A). The estuary is stratified (Figures 2B, 3A). Neither fully oceanic nor fully riverine waters enter the channelized part of the estuary, x = 100-200 km. Over a tidal cycle, salinity contours travel ~9 km along-channel, though stable vertical stratification remains intact during all phases of the tide. In the vicinity of the embayment, x = 140-160 km, strong tidal mixing yields a homogeneous bottom layer that is 10-12 m thick in the thalweg (Figure 3B). Top to bottom salinity difference at the center of the domain is ~10. The along-channel structure of the tidally-averaged circulation reveals saline water flowing into the estuary near the bottom and relatively fresh water exiting the estuary at the surface (Figure 3A), consistent with observations and other modeling studies of estuarine exchange flow. The across-channel structure of the tidally-averaged circulation at the center of the domain reveals a three-layer fluid (Figure 3C). Across-channel circulation is symmetric about the thalweg. Tidally-averaged flow is towards the shallows of the channel at the surface and in the homogenous bottom layer and strongly towards the thalweg in a narrow layer from 2-7 m depth (Figure 3C).

All further discussions refer to the channel at x = 150 km. The tidal range is 1.3 m. Maximum along-channel velocities are 1.2 m s^{-1} during ebb and 1 m s^{-1} during flood (Table 2; Figures 4A, 5A). Maximum velocities occur at the surface during ebb (Figure 5A). During flood, maximum velocities occur subsurface, at ~6 m depth. A ~1 hour phase shift exists between the surface and bottom velocities on maximum flood, maximum ebb, and slack after ebb. Both the surface and bottom slack simultaneously after flood. The across-channel circulation is described as a three-layer flow, but varies in magnitude and structure over the tidal cycle (Figures 4B, 5B). Following Lerczak and Geyer (2004), we measure the strength of the across-channel circulation by calculating the across-channel average of the magnitude of the across-channel velocity at the center of the domain (x = 150 km):

$$\langle |v| \rangle = \frac{1}{A} \int |v| \, dA$$

where $|v|$ is the absolute value of the cross-channel velocity, v, and A is the cross-channel area (Figure 4B). Across-channel flows peak near slack after flood and, to a much lesser degree, near surface slack after ebb (Figure 4B). Note that the bottom has already been flooding for nearly 2 hours at this time. Again following Lerczak and Geyer (2004), we assess the potential for the across-channel flows to influence the along-channel estuarine circulation by a scaling of the magnitude of the across-channel flow over a tidal time scale to the width of the channel:

$$\frac{4\langle|v|\rangle}{\sigma B} \geq 1$$

where σ is the tidal time scale and B is the width of the channel. For the maximum across-channel flows (0.025 m s^{-1}, Figure 4B), the scale of across-channel advection over a tidal time scale ($(12.42 \text{ h} \times 3600 \text{ s})^{-1}$) is less than the half width of the channel (2500 m), ~0.89. Therefore, across-channel advection should not be important in the along-channel momentum balance. However, as discussed below, instantaneous across-channel velocities at discrete across-channel locations and depths can be twice to three times as large as the across-channel mean flows.

The vertical structures of the across-channel and vertical flow are analyzed at a location midway between the thalweg and northern boundary (Figures 5B-C). Across-channel flow in the nearly homogeneous bottom layer and in the near-surface layer is always towards the shallows (Figure 5B). However, the thickness, position, and magnitude of flow within the subsurface layer changes on different tidal phases. As shown in Figure 4B, across-channel flow is strongest (~0.078 m s^{-1}) near slack after flood (hour 6) and is directed towards the thalweg (Figure 5B). Vertical velocities are also largest and upward near slack (Figure 5C).

b. Dynamics

The terms of the across-channel momentum equation are analyzed at the same location midway between the thalweg and northern boundary (Figure 6). In many parts of the water column during various phases of the tide, a dominant balance of the across-channel momentum exists between vertical stress divergence due to viscous forces and the baroclinic pressure gradient, though the barotropic pressure gradient and nonlinear advective flux divergence ($u\frac{\partial v}{\partial x} + v\frac{\partial v}{\partial y} + w\frac{\partial v}{\partial z}$) are nonzero, but generally small (Figure 6). During maximum flood, this dominant balance holds in the bottom layer. In the subsurface layer, the baroclinic pressure gradient is larger than the vertical stress divergence and drives across-channel accelerations of the across-channel velocity. In the surface layer, the baroclinic pressure gradient exceeds the combination of nonlinear advective flux divergence (dominated by $v\frac{\partial v}{\partial y}$, not shown) and vertical stress divergence and leads to positive accelerations in the across-channel direction. During maximum ebb, the dominant balance between vertical stress divergence and the baroclinic pressure gradient persists near the bottom and in the subsurface layer. Again, accelerations of the across-channel velocity near the surface result from the baroclinic pressure gradient. During slack after flood, when across-channel flows are largest, the dominant balance is not consistent with depth. Except for at the bottom, where viscous forces reduce the v-momentum, the vertical stress divergence is small because along-channel velocities are small. In the subsurface layer, across-channel acceleration follows the baroclinic pressure gradient, which is partially balanced by advective flux divergence. During slack after ebb, across-channel velocities peak again, but are small compared to the magnitude of those during slack after flood. Acceleration of across channel flow follows the baroclinic pressure gradient, similar to slack after flood, except near the bottom, where vertical stress divergence dominates. Nonlinear advective flux divergence becomes important to the momentum balance after the peaking of the across-channel flows.

The prominent role of the baroclinic pressure gradient in the upper layers of the water column supports the idea that the across-channel circulation is largely driven by differential advection of the along-channel salinity gradient. In this scenario, salt is transported differing distances by horizontally sheared (in y) along-channel currents. Differential advection results in across-channel salinity gradients and baroclinic pressure gradients that largely govern the across-channel circulation. This process occurs in the subsurface layer on maximum flood and near the surface on maximum ebb. Higher salinity is found in the subsurface layer, at the depth of maximum flood velocities, and is apparent in the ballooning of subsurface salinity contours (Figure 3B). The prominent role of the vertical stress divergence in the well-mixed bottom layer is indicative of the importance of boundarymixing over the sloping bottom in creating across-channel salinity gradients. In this scenario, across-channel salinity gradients drive across-channel flows from the thalweg to the shoals, as observed. In the center of the channel, the primary circulation is laterally divergent in the surface and bottom layers and convergent in the interior. The across-channel circulation is strongly affected by the presence of the embayment and is the subject of discussion of the rest of this work.

4. Embayment dynamics

a. Circulation

The embayment circulation is spatially and temporally complex, though the along-channel structure of the tidally-averaged circulation is similar to that of the channel-only run. Saline waters flow into the estuary at the bottom and relatively fresh waters exit the estuary at the surface (Figure 7A). However, the along-channel distribution of salinity is slightly different than that of the channel circulation without the bay. For example, the salinity = 26 contour is shifted ~1 km west in the circulation with the bay (Figures 3A, 7A), indicating a potential weakening of the estuarine exchange flow. The dominant signature of the tidally-averaged embayment fields is elevated surface salinity compared to that of the adjacent channel, coupled with enhanced upward sloping of the isopycnals from the thalweg into the bay (Figures 7B, 8B). Tidally-averaged, across-channel flows are strongly into the embayment at the center of the domain and out of the embayment at its edges (Figure 8E). The tidally-averaged, across-channel circulation upstream (x = 145 km) and downstream (x = 155 km) of the embayment is largely unaffected by the embayment, though small signatures are visible in both the across-channel salinity and velocity (Figure 8). Away from the embayment, tidally-averaged flows are towards the shallows in the surface and bottom layers and towards the thalweg in the subsurface layer, as described in the previous section.

Along-channel velocities are similar to those in the channel-only run (Figures 4A, 9A). However, both the evolution in time of the magnitude of across-channel flow and the magnitude itself are different (Figures 4B, 9B). Across-channel flows peak twice per tidal cycle. Both peaks are of the same order or larger than the maximum magnitude of across-channel flows in the channel-only run. For the maximum across-channel flows, the scale of across-channel circulation over a tidal time scale is greater than the half width of the channel, ~1.25. Therefore, we expect across-channel advection to be important to both the along-channel and across-channel momentum balances. Indeed, nonlinear advective flux divergence is important during all phases of the tide and is balanced by the barotropic and baroclinic pressure gradients (Figure 10). During slack tides, advection dominates above 5 m depth, but is negligible below. The opposite is true during maximum flood and ebb.

Twice per tidal cycle, cyclostrophic eddies are observed to form in the embayment and to eject from the embayment into the channel, where they are transported along-channel by the ambient channel velocity (Figure 11). In Figure 11, four panels depict the evolution of surface salinity over ~5 hours of the tidal cycle. In the first panel, the channel is flooding and the development of an eddy inside the embayment is expressed by the doming of salinity contours. High salinity water is drawn into the bay from depth in the channel. The eddy has positive vorticity due to the shear in along-channel velocity at the northern boundary ($-\frac{\partial u}{\partial y} > 0$). In the second panel, the channel is approaching slack after flood. The eddy is at its maximum size during this time; roughly the scale of the embayment. Vertical mixing within the bay has distributed salt through the water column. In the third panel, at slack after flood, the eddy is ejected from the embayment at its western edge. Ejection of well-mixed eddies results in injection of anomalously high salinity water with positive vorticity into the channel surface layer. In the fourth panel, the ebb eddy is developing in the embayment. The ebb eddy has negative vorticity. The surface salinity signature of the ejected flood eddy is still present in the channel ~20 km from the embayment and ~6 hours after ejection. The flood eddy maintains its radius of ~1 km during all stages of its life cycle. Eddy formation and ejection occurs twice per tidal cycle: relatively high salinity waters are transferred from depth in the channel to the surface during both flood and ebb. However, there are asymmetries between these two phases. In contrast to the flood eddy described above, the ebb eddy has a tighter core upon ejection and persists in the channel for ~10 km only as a disturbance adjacent to the northern boundary (first panel, Figure 11).. A conceptual schematic of eddy formation and ejection associated with tidal hours is presented in Figure 12.

b. Salinity anomaly analysis

The elevated salinity of the embayment relative to the adjacent channel is critical to understanding the overall effect of the embayment on the estuarine dynamics. To understand the processes creating this anomaly, we document the injection, mixing, and ejection of embayment salt through bulk measures. In the following figures, the abscissa is tidal hours, as in Figure 4. Referring back to Figure 4A, the tidal cycle begins (tidal hour 1) during slack after ebb, though there is a large phase shift between surface and bottom along-channel velocities. At tidal hour 3, along-channel flows reach maximum flood. At tidal hour 6, the channel is at slack after flood. Lastly, at tidal hour 9, along-channel flows reach maximum ebb. First, we describe the evolution of the bulk measures independently. Second, their evolution is related to eddy dynamics.

In Figure 13, bay-averaged salinity and the time derivative of bay-averaged salinity are presented. The conceptual schematic suggests that the west and east halves of the bay act out of phase (i.e., injection occurs through the west side of the embayment mouth during flood as the ebb eddy is ejected through the east side). Salinity must also be entering the embayment at depth, since it is higher than the surface salinity. Thus, we decompose bay-averaged salinity into four quadrants: bottom west (x < 150 km, depth > 2.5 m), surface west (x < 150 km, depth < 2.5 m), bottom east (x > 150 km, depth > 2.5 m), surface east (x > 150 km, depth < 2.5 m; Figure 13c). Bay-averaged salinity decreases for more than 2 hours from slack after ebb until maximum flood. From maximum flood until slack after flood, bay-averaged salinity increases. During slack after flood, bay-averaged salinity decreases for ~1 hour. Then, until slack after ebb, bay-averaged salinity increases. The increase during ebb is not monotonic (Figure 13B). The decreases on opposite phases of the tide are very clearly asymmetric – compare salinity decreases during tidal hours 12-3 and tidal hours 6.5-7.5. It is apparent that the west and east sides of the bay are out of phase (Figure 13C). At some tidal hours, the bottom and surface are out of phase.

The change in total salt of the embayment must be equal to the salt advective flux (SAF) across the mouth of the embayment.

$$\frac{d}{dt}\int_V S\,dV = SAF$$

where

$$SAF = \int_A vS\,dA$$

t is time, S is salinity, V is the volume of the bay, v is the across-channel velocity, and A is the area of the mouth of the embayment.

$$d\int_V S\,dV = SAF$$

To consider salinity instead of total salt, it is convenient to divide both sides by the bay volume.

$$\frac{1}{V}d\int_V S\,dV = AF$$

where AF is the salt advective flux normalized by bay volume (Figure 14A).

$$AF = \frac{ASF}{V}$$

AF can be partitioned into contributions from the time derivative of bay volume and the time derivative of salinity by the chain rule (Figure 14A):

$$AF = \frac{1}{V}V\frac{dS}{dt} + \frac{1}{V}S\frac{dV}{dt}.$$

AF is strongly a function of the time derivative of bay volume. Bay volume increases due to water entering the bay, and therefore AF is positive during this time period (Figure 14A,C). However, the deviations in AF from that associated with bay volume changes alone reveal times when the salinity of the bay is altered. The advective flux deviates from changes in bay volume most strongly during tidal hours 1 and 2, when bay volume is increasing, but salinity is decreasing. In Figure 14B, AF is decomposed into quadrants as above. AF is large and out of phase between the west and east sides of the mouth of the embayment. However, AF is also clearly out of phase at the surface and bottom.

Bay-integrated salt diffusive flux (DF) describes vertical mixing of salt in the embayment:

$$DF = -\frac{1}{V}\int K_s \frac{\partial S}{\partial z}\, dV$$

where K_s is the vertical diffusivity coefficient for salt and $\frac{\partial S}{\partial z}$ is stratification. Time series of DF, bay-averaged K_s, and bay-averaged -$\frac{\partial S}{\partial z}$, estimated as the difference between the surface and bottom, are presented in Figure 15. The DF was not observed to vary when decomposed into quadrants of the embayment, indicating that mixing is large or small throughout the bay simultaneously. Bay-integrated DF and bay-averaged K_s peak twice per tidal cycle (Figure 15A,B) during times when bay-averaged salinity is increasing (Figure 13A). Stratification also peaks twice per tidal cycle (Figure 15C) following large decreases in salinity (Figure 13A).

Now, we relate these bulk measures to eddy formation and ejection. Between tidal hours 12 through 2, the channel is transitioning from slack after ebb to maximum flood. Waters at depth are already near maximum flood velocities (Figure 4A). The ejection of the ebb eddy is marked by decreasing salinity of the east side of the bay (Figure 13A,C) and large negative advective fluxes through the east side of the mouth (Figure 14B,C). The salinity decrease is uniform through the surface and bottom, indicating that the ejecting waters are well-mixed. This is corroborated by the small stratification at tidal hour 12 (Figure 15C). Positive overall advective fluxes during this time are driven by bay volume increases concentrated in the west side of the bay (Figure 14A), although the deviation from the volume term indicates the relatively large influence of changing salinity.

Flood eddy formation occurs shortly after the start of ebb eddy ejection (tidal hour 1), indicated by salinity increases across the west side of the mouth (Figure 13C). As a result, bay-averaged salinity increases from maximum flood to slack after flood (Figure 13A), despite decreasing bay volume (Figure 14A,C).

The net effect of the circulation is anomalously high salinity in the embayment relative to the surface waters of the adjacent channel. We quantify the salinity anomaly (S') as:

$$S' = \bar{S}_{bay} - \bar{S}_{chan}$$

where $\bar{S}_{bay}$ is the bay-averaged salinity and $\bar{S}_{chan}$ is the channel-averaged salinity. We calculate $\bar{S}_{chan}$ over the along-channel distance corresponding to the mouth of the embayment and from the surface to 5 m depth. For the base run, radius = 1.5 km, the bay is anomalously salty compared to the channel over most of the tidal cycle (Figure 16). Integrated over the tidal cycle, the salinity anomaly is large and positive. This unit of measure is used to describe the strength of the circulation in the bay radius sensitivity studies below.

c. Dynamics

The terms of the across-channel momentum equation are analyzed along the mouth of the embayment (Figure 17). At all phases of the tide, the primary balance is between the barotropic pressure gradient and advective flux divergence. The advection term is dominated by divergence of the across-channel momentum flux. The vertical stress divergence and baroclinic pressure gradient are small when averaged over the mouth, but are important for particular quadrants of the mouth (Figure 18). At the bottom, the vertical stress divergence becomes important and, in conjunction with the advective flux divergence, balance the barotropic pressure gradient. At the surface, the vertical stress divergence is negligible. The baroclinic pressure gradient is not large anywhere at any time, but briefly becomes important when eddies have stabilized and salt advection across the mouth is near zero (tidal hours 4 and 10; Figure 14).

Ejection events, both large and small, coincide with reversals in the sign of the barotropic pressure gradient (Figures 13A, 17). The overtide signal of the barotropic pressure gradient averaged over the mouth appears to be a result of the phase shift between the west and east sides of the embayment (i.e. maxima of the terms, though opposite, are lagged). Asymmetry in the along-channel flood and ebb tides results in asymmetry in the bay forcing.

5. Sensitivity to embayment geometry

The radius of the embayment was varied over a range defined by a factor of two smaller and larger than the base run to investigate the effect of embayment geometry on circulation. Experiments included radii = 0.75 km, 1 km, 2 km, 2.5 km, and 3 km (Table 1). The radius of the embayment was precluded from reaching the width of the channel by numerical limitations imposed at the boundaries. With a larger nest such that the boundaries are farther from the embayment, embayment geometries where the radius is equal to or larger than the width of the channel could be explored.

With all embayment radii, eddies were observed to form on both flood and ebb tides. Elevated salinity within the bay relative to the adjacent channel is obtained in all runs, as is the observed asymmetry in the evolution of bay-averaged salinity over flood and ebb. However, the magnitude of the salinity anomaly integrated over a tidal cycle varies with embayment radius. Despite the limited range of runs, we observe an inverse relationship between the radius and salinity anomaly. As embayment radius increases, the magnitude of the salinity anomaly decreases (Figure 18). With larger bay radii, the barotropic pressure gradients are smaller and are balanced by smaller across-channel advection, leading to less transport of salt into the embayment.

6. Final remarks

This work investigates the tidal dynamics of a shallow embayment adjacent to a long, linear estuary. During both flood and ebb tides, a cyclostrophic eddy is created inside the embayment and relatively high salinity water is transported into the bay from the well-mixed bottom layer of the channel. Large barotropic pressure gradients are created at the mouth of the embayment by the phasing of the bay response to the free surface elevation of the channel. Barotropic pressure gradients are balanced by large across-channel advective flux divergences. Vertical mixing within the bay breaks down the stratification resulting from high salinity waters preferentially entering the bay near the bottom. As a result of mixing, relatively high salinity water is transported out of the bay throughout the water column during eddy ejection on slack tides. The surface signature of vorticity and elevated salinity of the eddy persists downstream of the embayment on both phases of the tide. The tidally-averaged effect of this circulation is anomalously high salinity within the embayment relative to the adjacent channel surface waters. The magnitude of the salinity anomaly integrated over a tidal cycle varies inversely with the embayment radius, for the range of radii considered here. As embayment radius increases, the magnitude of the barotropic pressure gradient decreases. Though cyclostrophic eddies were observed for all bay radii considered, it is possible that increasingly large radii would not support the barotropic pressure gradient which maintains the eddies. At very small embayment radii, the barotropic pressure gradient controlling the salt advective flux across the mouth would become insignificant as bay responses to the free surface elevation of the channel would not lag in time.

The dynamics responsible for fluxes into and out of the embayment are independent of the across-channel structure and circulation. However, we expect that different across-channel circulation would alter the magnitude of the bay salinity anomaly, though not explored in this work. The salt advective flux across the mouth of the embayment is sensitive to channel stratification and bay depth, which both influence the salinity of the water drawn into the bay from the channel subsurface. Additionally, stratification modifies the across-channel circulation (Chant and Wilson, 1997; Lacy and Monismith, 2001; Lerczak and Geyer, 2004; Cheng et al., 2009), and thus also the across-channel salt flux. The competing effects of stratification to suppress (Lerczak and Geyer, 2004; Chant and Wilson, 1997) or enhance (Lacy and Monismith, 2001) across-channel circulation makes it difficult to predict the response of the embayment features described here to stratification changes. However, the overall circulation pattern would remain the same, as eddy formation is driven by the interaction of the along-channel flow with the boundary and salt injection and ejection from the bay are driven by the barotropic pressure gradient associated with the free surface elevation of the channel.

Eddies have been observed to form from the interaction of tidal currents with islands, headlands (Signell and Geyer, 1991; Geyer, 1993; Chant and Wilson, 1997), and shoals (Pingree, 1978). Both the enhanced lateral circulation and the persistence of eddies inside the embayment observed in this study are expected to be important for the distribution of salt and sediment within the estuary (Geyer, 1993). Indeed, preliminary model simulations not discussed here suggest that fine sediments are suspended throughout eddy cores and are transported out of the embayment on eddy ejection. Furthermore, preliminary model simulations suggest deposition of fine sediments in the center of the embayment, consistent with expectations for sediment trapping in residual eddies (Heathershaw and Hammond, 1980).

Lastly, the influence of the enhanced across-channel circulation on the momentum balance of the along-channel estuarine circulation was not explored. However, a scaling of the across-channel advection over a tidal cycle relative to the channel half-width suggests that the across-channel circulation of the embayment is an important component of estuarine circulation. An assessment of the along-channel momentum balance could confirm the importance of across-channel advection and demonstrate that features with relatively small geometric scales compared to the estuary length are critical parts of the overall circulation.

Limited data from Corte Madera Bay, the embayment in San Francisco Bay which motivated this study, show that the embayment is salty relative to the channel at times, though not always (Lacy and Hoover, 2011). However, observations are spatially limited and unable to identify mechanisms responsible for the anomaly. The dynamics detailed here are analogous to those present in other tidally-forced systems (e.g., flow past headlands) with stratification (e.g., curving or straight channels). However, the transport of salt by enhanced across-channel circulation in the vicinity of estuarine embayments of this size has not been previously described, but has implications for the transport of other tracers, such as sediment or pollutants, and preferred habitats of estuarine species.

REFERENCES

Basdurak, N.B. and A. Valle-Levinson, 2012. Influence of advective accelerations on estuarine exchange at a Chesapeake Bay Tributary. *Journal of Physical Oceanography*, 42, doi:10.1175/JPO-D-11-0134.1.

Chant, R.J. and R.E. Wilson, 1997. Secondary circulation in a highly stratified estuary. *Journal of Geophysical Research*, 102, 23207-23215.

Chen, S.N. and L.P. Sanford, 2009. Lateral circulation driven by boundary mixing and the associated transport of sediments in Idealized partially mixed estuaries. *Continental Shelf Research*, 29, 101-118, doi:10.1016/j.csr.2008.01.001.

Cheng, P., R.E. Wilson, R.J. Chant, D.C. Fugate, and R.D. Flood, 2009. Modeling influence of stratification on lateral circulation in a stratified estuary. *Journal of Physical Oceanography*, 39, doi:10.1175/2009JPO4157.1.

Kalkwijk, J.P.T. and R. Booij, 1986. Adaption of secondary flow in nearly-horizontal flow. *Journal of Hydraulic Engineering*, 24, 19-37.

Kantha, L.H. and C.A. Clayson, 1994. An improved mixed layer model for geophysical applications. *Journal of Geophysical Research: Oceans*, 99, 25235-25266, doi:10.1029/94JC02257.

Geyer, W.R., 1993. Three-dimensional tidal flow around headlands. *Journal of Geophysical Research*, 98, 955-966.

Haidvogel, D.B., H.G. Arango, K. Hedstrom, A. Beckmann, P. Malanotte-Rizzoli, and A.F. Shchepetkin, 2000. Model evaluation experiments in the North Atlantic Basin: simulations in nonlinear terrain-following coordinates. *Dynamics of Atmospheres and Oceans*, 32, 239-281, doi:10.1016/S0377-0265(00)00049-X.

Hansen, D.V. and M. Rattray, 1965. Gravitational circulation in straits and estuaries. *Journal of Marine Research*, 23, 104-122.

Heathershaw, A.D. and F.D.C. Hammond, 1980. Secondary circulations near sand banks and in coastal embayments. *Ocean Dynamics*, 33, 135-151.

Lacy, J.R. and S.G. Monismith, 2001. Secondary currents in a curved, stratified, estuarine channel. *Journal of Geophysical Research*, 106, 31283-31302.

Lacy, J.R. and D.J. Hoover, 2011. Wave exposure of Corte Madera Marsh, Marin County, California – a field investigation. U.S. Geological Survey Open-File Report 2011-1183.

Lerczak, J.A. and W.R. Geyer, 2004. Modeling the lateral circulation in straight, stratified estuaries. *Journal of Physical Oceanography*, 34, 1410-1428.

Nunes, R.A. and J.H. Simpson, 1985. Axial convergence in a well-mixed estuary. *Estuarine Coastal Shelf Science*, 20, 637-649.

Phillips, O.M., 1970. On flows induced by diffusion in a stably stratified fluid. *Deep-Sea Research*, 17, 435-443.

Pingree, R.D., 1978. The formation of the Shambles and other banks by tidal stirring of the seas.

Rozovski, I.L., 1957. *Flow of Water in Bends of Open Channels*. Is. Program for Sci. Transl. Jerusalem.

Shchepetkin, A.F. and J.C. McWilliams, 2005. The Regional Ocean Modeling System (ROMS): A split-explicit, free-surface, topography-following coordinates ocean model. *Ocean Modelling*, 9, 347-404.

Signell, R.P. and W.R. Geyer, 1991. Transient eddy formation around headlands. *Journal of Geophysical Research*, 96, 2561-2575.

Smith, R., 1976. Longitudinal dispersion of a buoy contaminant in a shallow channel. *Journal of Fluid Mechanics*, 78, 677-688.

Run	*Radius (km)*
1	1.5
2	0.75
3	1
4	2
5	2.5
6	3

Table 1. Embayment radius sensitivity studies. Run 1 is the base run.

Tidal Stage	*Tidal Hour*
max flood	3
slack flood	6
max ebb	9
slack ebb	12

Table 2. Tidal stage and hours.

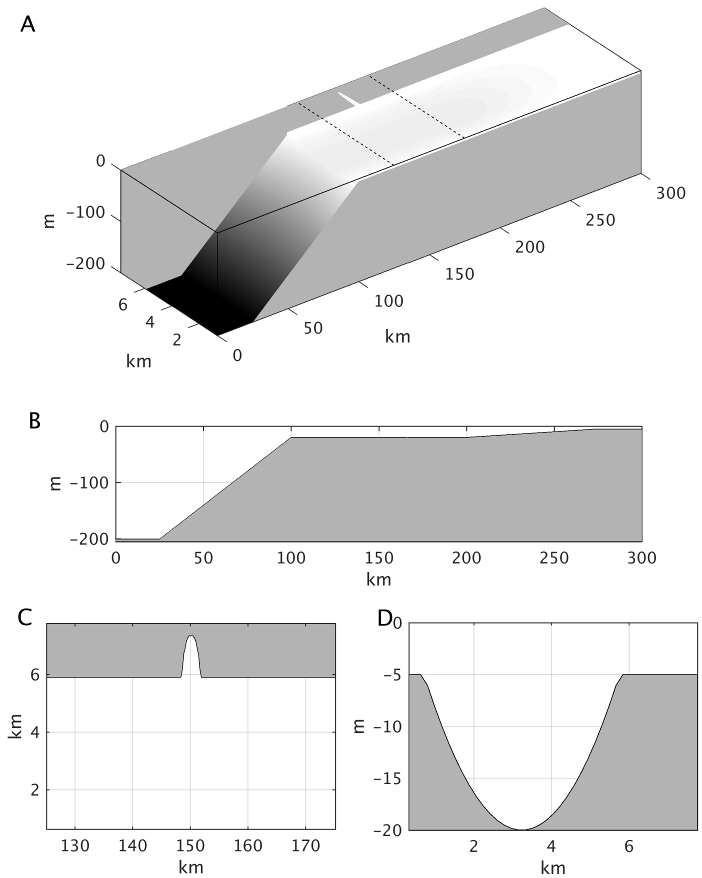

Figure 1. Model domain. Note that the aspect ratio changes in each figure and is not 1. A) The domain is a long, linear estuary with a small embayment extending from the northern boundary. Dashed lines mark the western and eastern boundaries of the nested grid. B) From the oceanic to riverine ends, the along-channel bathymetry progresses from deep to a parabolic channel to shallow. C) Inset of the nested grid with the embayment from the base run, radius = 1.5 km. The aspect ratio is not 1. D) Across-channel bathymetry is a parabolic channel with a shallow (5 m) shelf through the embayment.

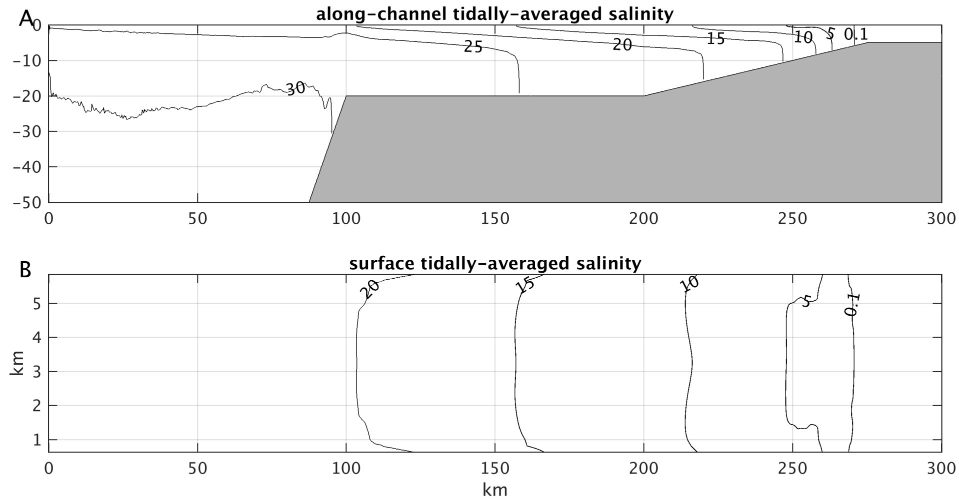

Figure 2. Tidally-averaged features of the outer domain. A) Tidally-averaged along-channel salinity contours. The contour interval is 5, except for the contour of salinity = 0.1, which denotes the extent of the salinity intrusion. B) Tidally-averaged surface salinity contours. Same as in A.

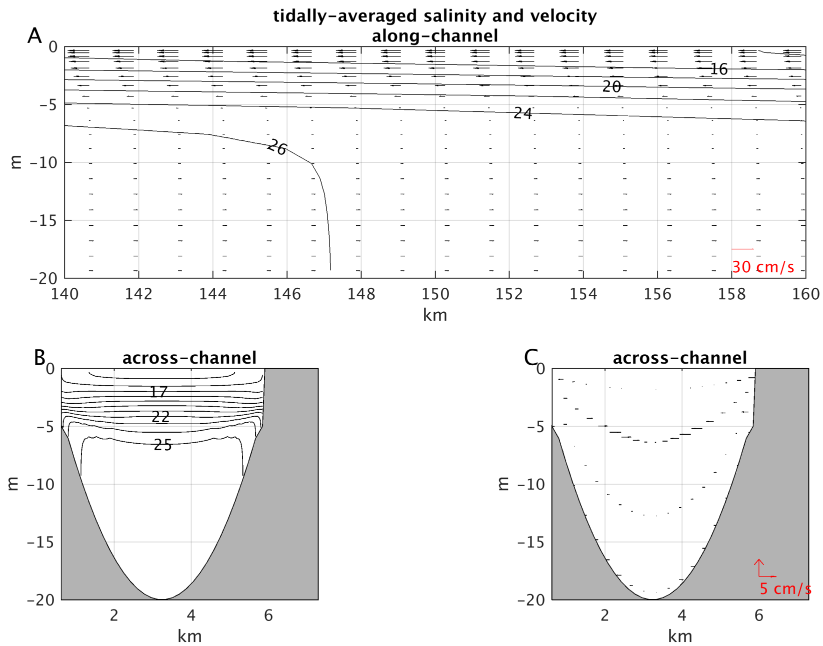

Figure 3. Tidally-averaged features of the channel. A) Tidally-averaged along-channel salinity contours and along-channel velocity. The contour interval is 2. B) Tidally-averaged across-channel salinity contours, looking downstream. The contour interval is 1. C) Tidally-averaged across-channel velocity.

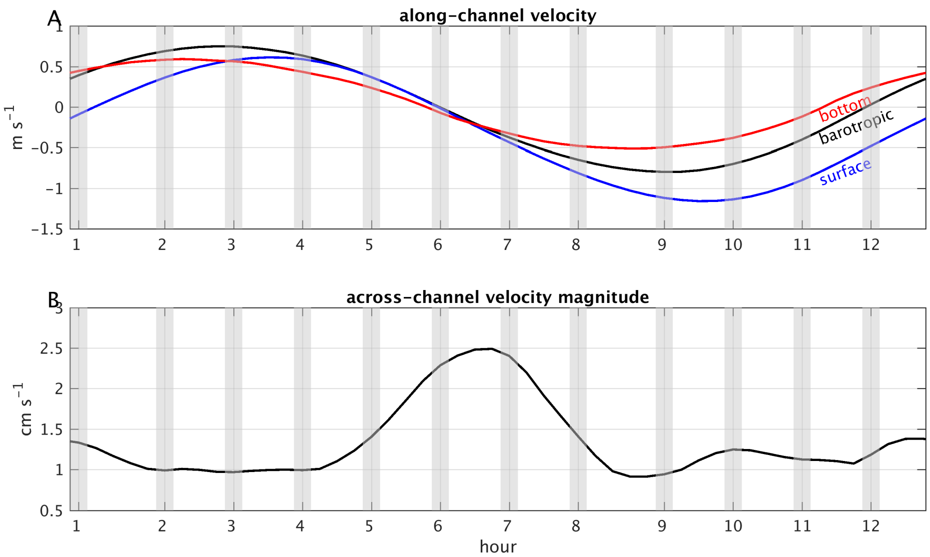

Figure 4. Measures of the along-channel and across-channel velocity. The x-axes mark tidal hours, which are roughly spaced at 12.42 hour/12 intervals. The ticks are coincident with the nearest model output to the tidal hour. The vertical gray shading indicate the 15 minute-window over which the variables were averaged. A) Surface, bottom, and barotropic along-channel velocities in the thalweg over a tidal cycle. B) Across-channel average magnitude of the across-channel velocity over a tidal cycle.

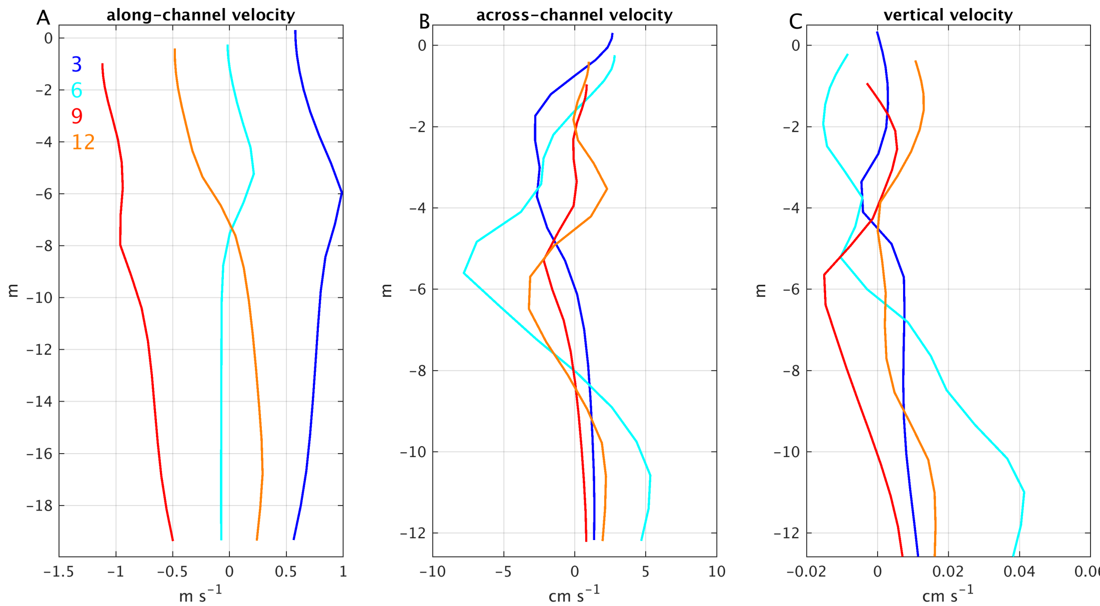

Figure 5. Vertical profiles at the along-channel center of the domain, x = 150 km, midway between the thalweg and northern boundary of the A) along-channel, B) across-channel, and C) vertical velocities during maximum flood (hour 3), slack after flood (hour 6), maximum ebb (hour 9), and slack after ebb (hour 12).

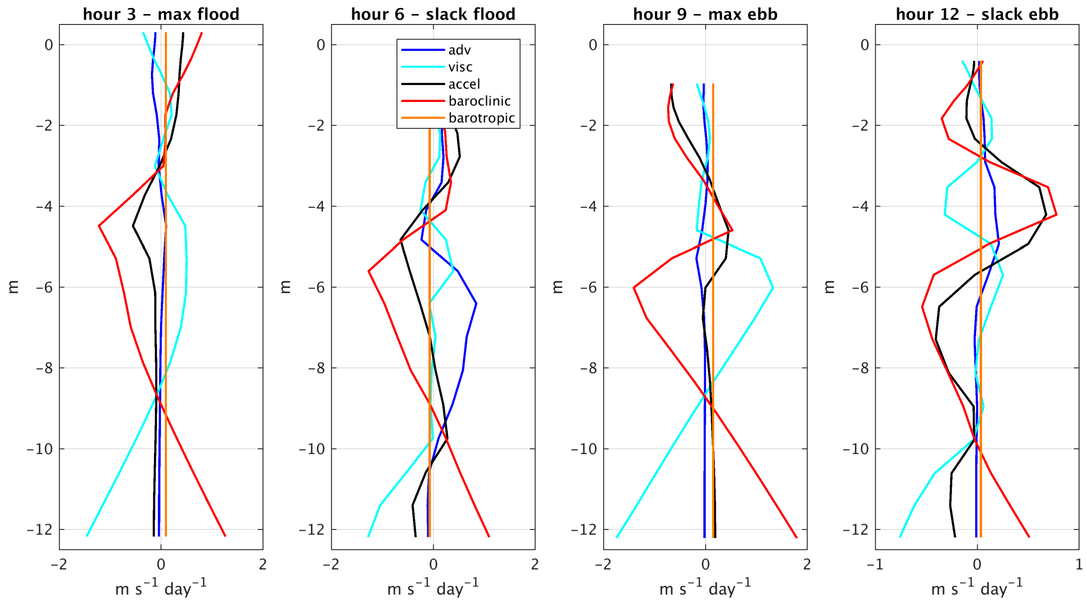

Figure 6. Vertical profiles of the terms of the v-momentum balance at the along-channel center of the domain, x = 150 km, midway between the thalweg and northern boundary during maximum flood, slack after flood, maximum ebb, and slack after ebb. Adv is nonlinear advective flux divergence, visc is vertical stress divergence, accel is time rate of change, baroclinic is the baroclinic pressure gradient, and barotropic is the barotropic pressure gradient.

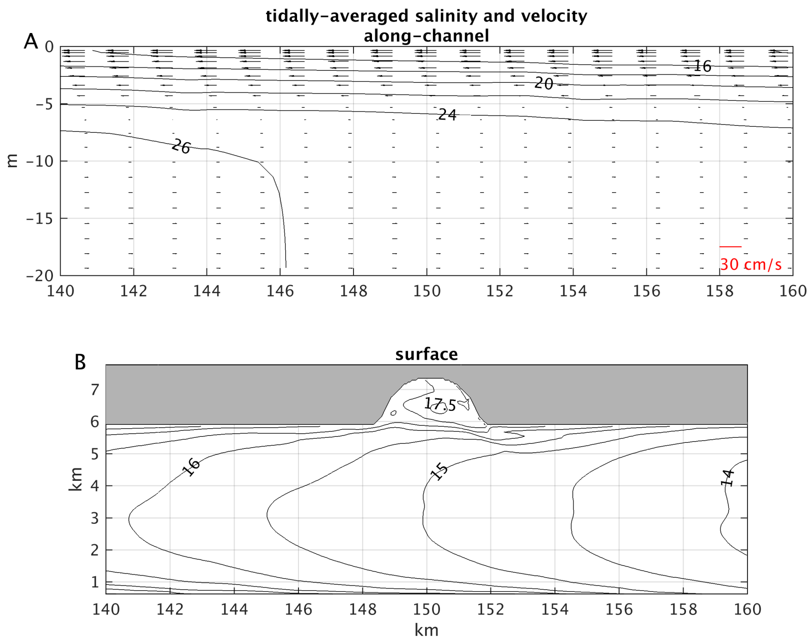

Figure 7. Tidally-averaged features of the channel and embayment. A) Tidally-averaged along-channel salinity contours and along-channel velocity. The contour interval is 2. B) Tidally-averaged surface salinity contours. The contour interval is 0.5.

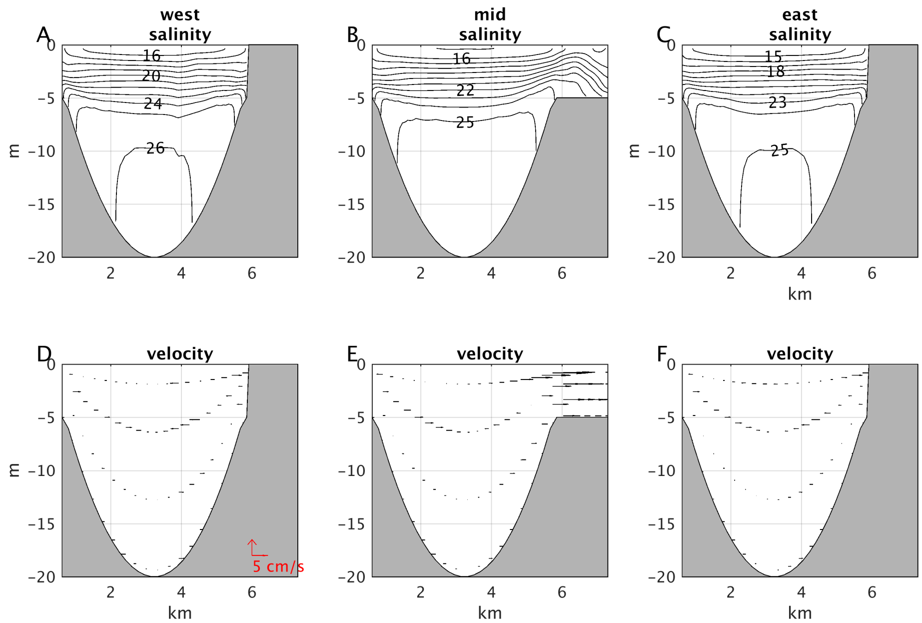

Figure 8. Tidally-averaged across-channel salinity and velocity at three along-channel locations, looking west. The salinity contour interval is 1. A and D) x = 145 km. B and E) x = 150 km, along the axis of the embayment. C and F) x = 155 km.

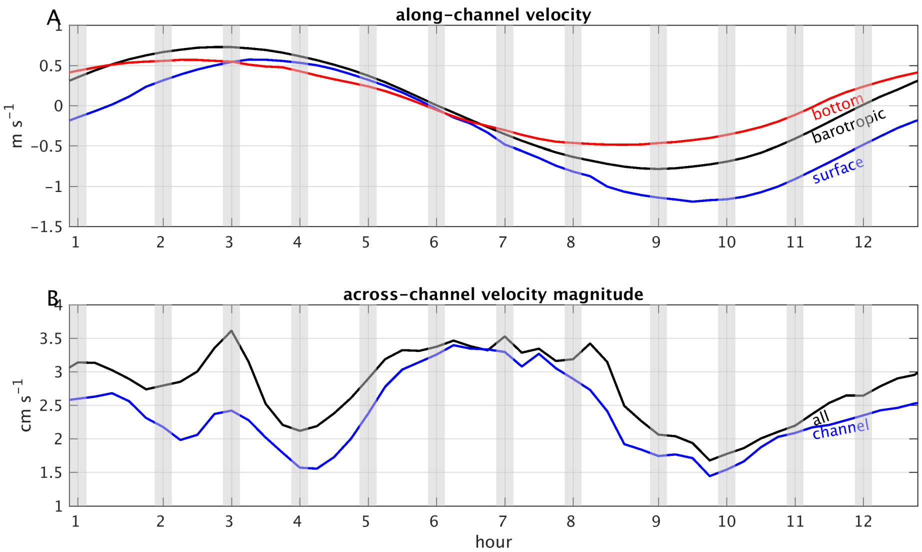

Figure 9. Same as Figure 4, but for the domain including the embayment. In 9B, the blue line indicates an across-channel average over only the channel, not including the embayment.

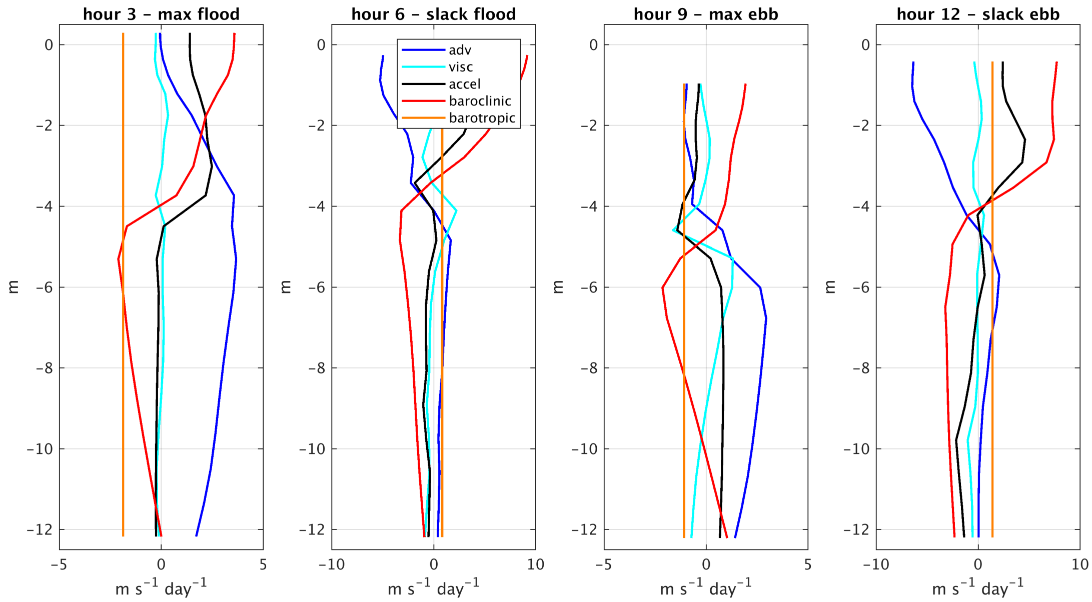

Figure 10. Same as Figure 6, but for the domain including the embayment. Legend is as in Figure 6.

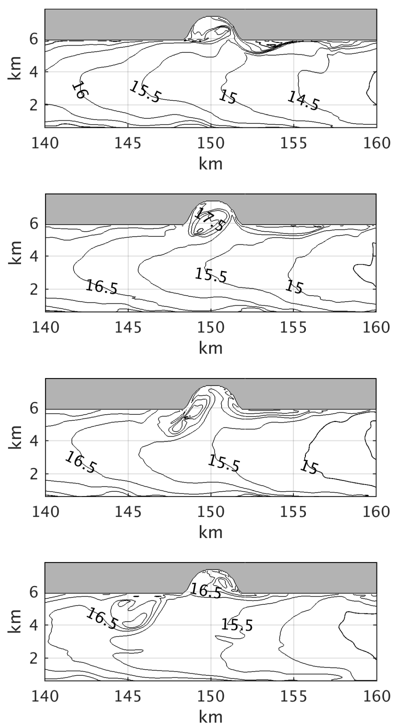

Figure 11. Surface salinity contours during the development and ejection of an eddy on flood tide. The series spans 5 tidal hours. The contour interval is 0.5.

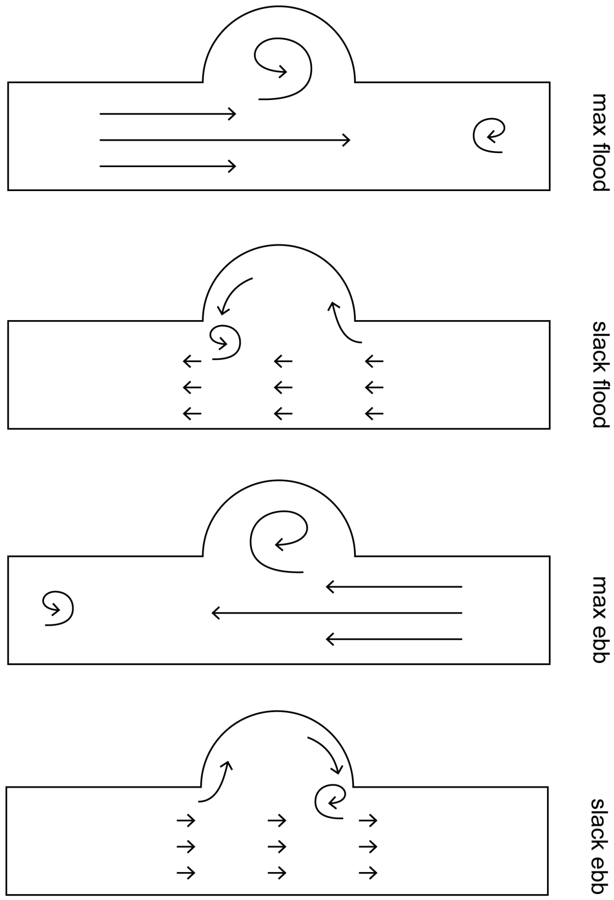

Figure 12. Conceptual schematic of eddy formation in the embayment during tidal maxima and ejection from the embayment during tidal slack. The eddies are composed of higher salinity waters than the adjacent channel surface.

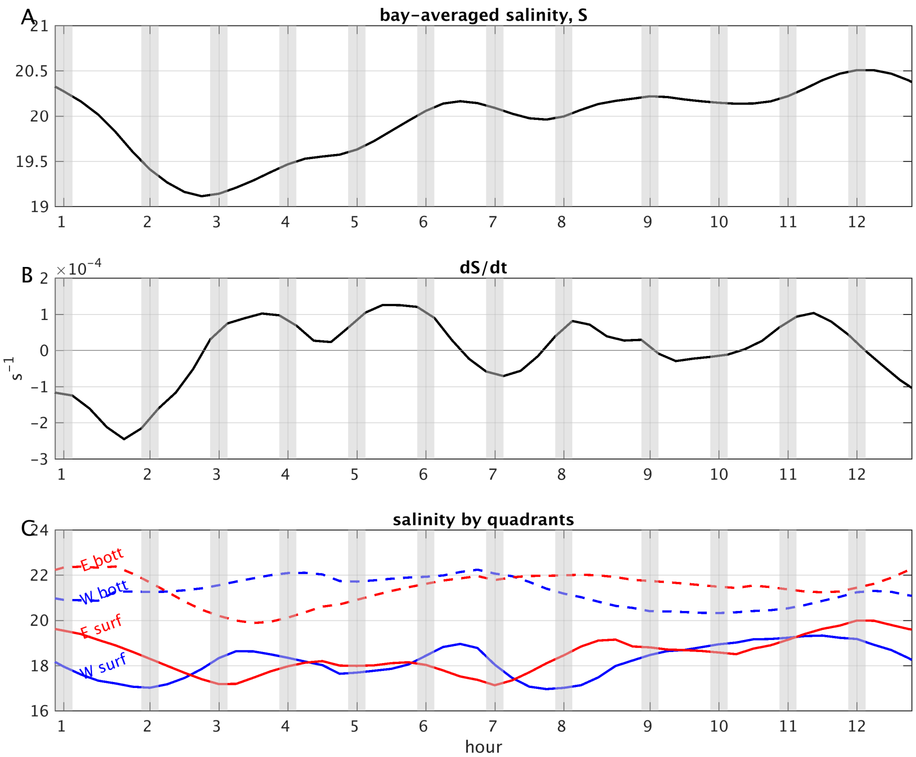

Figure 13. Time series of A) bay-averaged salinity, B) the time derivative of the bay-averaged salinity, and C) bay-averaged salinity decomposed into four quadrants: bottom west, surface west, bottom east, surface east. The x-axis and shading are as in Figure 4.

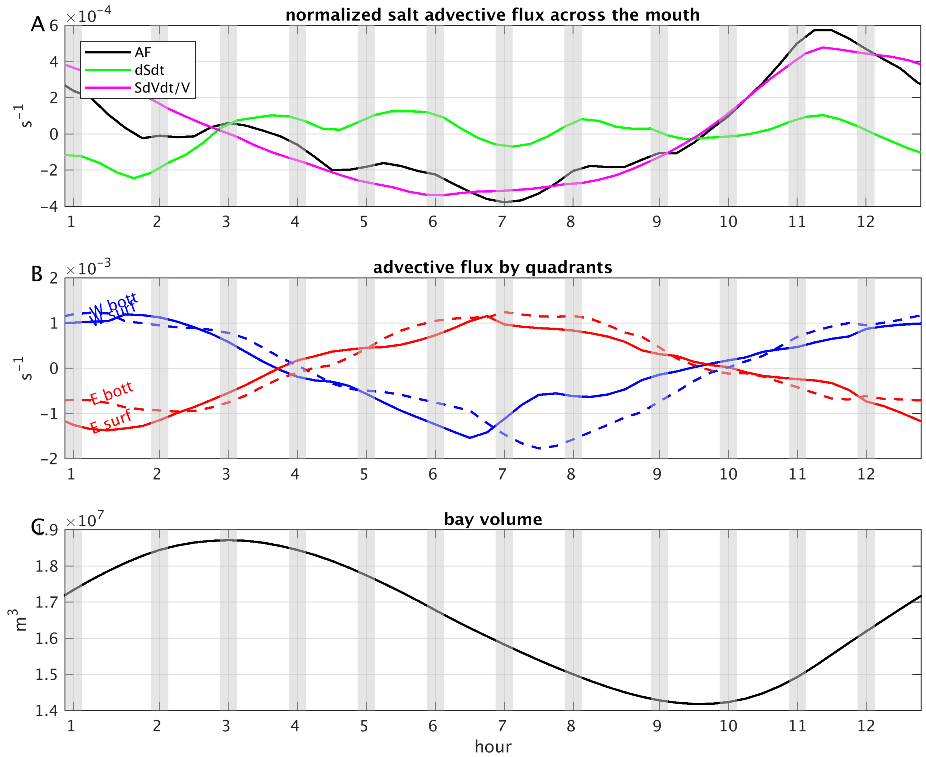

Figure 14. Time series of salt advective flux across the embayment mouth, normalized by the bay volume, decomposed into A) variations associated with changes in salinity (S), $\frac{\partial S}{\partial t}$, and volume ($V$), $S\frac{\partial V}{\partial t}$, normalized by the bay volume and B) four quadrants: bottom west, surface west, bottom east, surface east. C) Time series of the bay volume. The x-axis and shading are as in Figure 4.

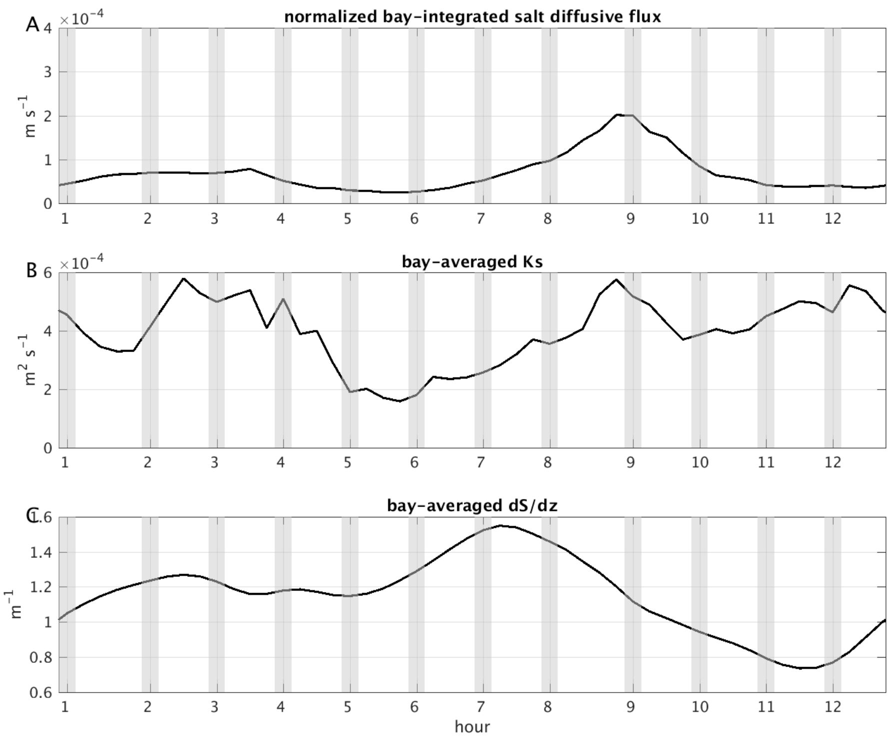

Figure 15. Time series of A) bay-integrated salt diffusive flux, normalized by the bay volume, B) bay-averaged salt diffusivity coefficient, K_s, and C) bay-averaged stratification, $\frac{\partial S}{\partial z}$. The x-axis and shading are as in Figure 4.

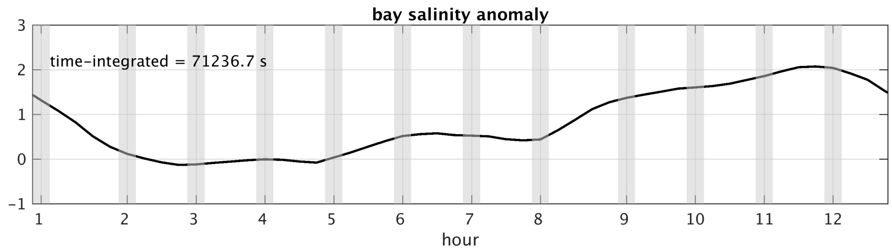

Figure 16. Time series of the salinity anomaly of the embayment relative to the upper layer of the adjacent channel.

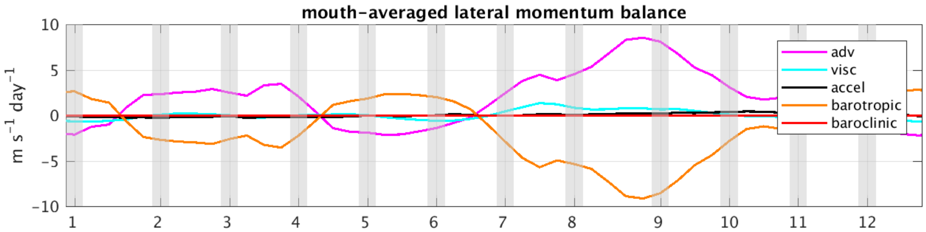

Figure 17. Time series of the terms of the across-channel momentum balance averaged over the embayment mouth. Adv is nonlinear advective flux divergence, visc is vertical stress divergence, accel is time rate of change, barotropic is the barotropic pressure gradient, and baroclinic is the baroclinic pressure gradient.

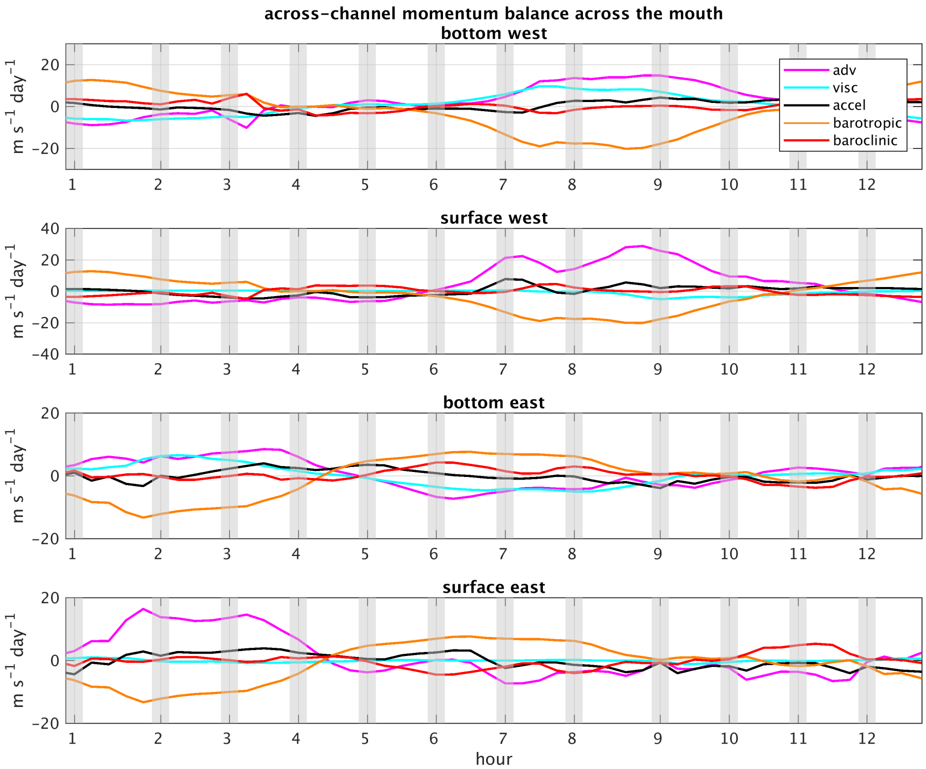

Figure 18. Time series of the terms of the across-channel momentum balance averaged over the embayment mouth, decomposed into four quadrants. Legend is as in Figure 17.

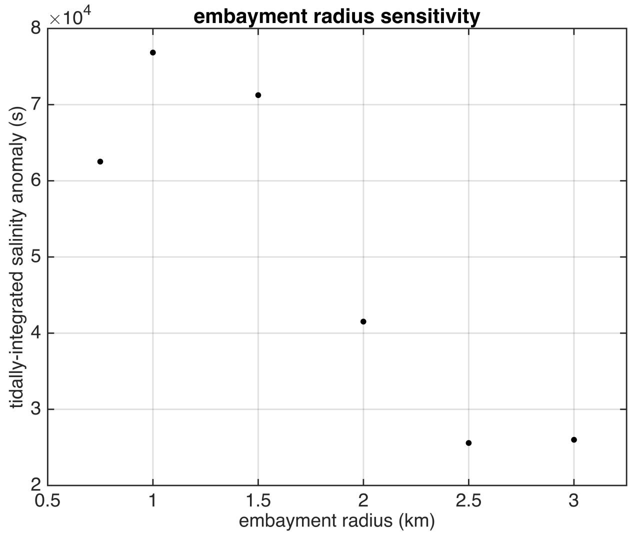

Figure 19. Relationship between the embayment radius and the tidally-integrated, bay-averaged salinity anomaly relative to the channel surface layer.

CHAPTER FIVE
CONCLUSION

Prediction of coastal processes and hazards at present and into the future requires the use of state-of-the-art modeling techniques to simulate the complex relationships between variables of interest, such as winds and waves or strong currents and salt. These relationships are difficult to identify and predict through observational records alone, which are sparse in space and time. Furthermore, the nonstationarity of relationships in time necessitates time-varying fields, which are difficult to obtain with observations, or statistical techniques, which are often limited in success by the available data. In this dissertation, improved modeling techniques for the projection of nearshore waves by atmospheric fields were developed and implemented. Additionally, a numerical model was used to simulate tidal flow past a shallow estuarine embayment. All three studies of this dissertation were motivated by the increasing need for a robust understanding of coastal processes and hazards. In Chapters 2 and 3, coastal hazards refer to coastal flooding and erosion due to changing wave conditions as a result of climate change. In Chapter 4, coastal hazards refer to marsh and habitat vulnerability in the face of sea level rise and limited sediment supply to estuaries.

In Chapter 2, an improved statistical downscaling method was developed for the prediction of deep-water waves by synoptic atmospheric circulation patterns. Statistical downscaling methods based on linear or nonlinear relationships between variables are often limited by several factors: 1) the representation of wave travel time, 2) the oceanic area over which wave generation is important, and, in the case of linear techniques, 3) the inability to include all nonlinearities in a random error function. In large ocean basins where waves are generated in multiple discrete locations and may travel weeks before arriving at the coast, factors 1 and 2 are particularly limiting. This work builds upon a statistical downscaling technique that models the nonlinear relationship between representative sea level pressure patterns and deep-water waves. The technique has been used extensively in relatively small ocean basins such as the Mediterranean and Atlantic Oceans. However, application to the Pacific Ocean resulted in markedly lower success in the prediction of waves, specifically wave direction. The most notable improvement implemented here was partitioning of the wave spectra into wave families, which were defined by spectral peaks and a wave speed to wind speed ratio. The individual partitions of the spectra relate to waves generated in discrete areas of the ocean basin. The second improvement to the statistical downscaling technique was the incorporation of a time lag in the relationship between sea level pressure and waves based on spatially-varying wave travel time.

Application of this improved method to locations with multimodal wave spectra (e.g., Southern California), indicating multiple wave generation areas, yielded improved wave prediction metrics over previous methods. Errors associated with wave direction have room for growth, but still represent an improvement. A potential source of error in the method is the definition of wave travel time. To calculate wave travel time, we estimated wave speed based on the mean wave period. It is likely that using this method, some wave energy is not properly linked in time to the wave-generating sea level pressure patterns. A further improvement to this method through the use of a range of wave periods to calculate travel times would likely yield smaller errors. A second source of error is in the wave spectra partitioning algorithm, which was suspected to incorrectly defined seas during shifty wind patterns. Improvement of the algorithm is not within the scope of this work.

In Chapter 3, a hybrid statistical-dynamical method was implemented to predict nearshore waves based on the transformation of deep-water waves predicted in Chapter 2 (and other related work) over the complex shelf bathymetry of the Southern California Bight. Previous modeling and observational studies suggested significant alongshore variability in nearshore wave conditions over small spatial scales. An investigation into the causes of the alongshore variability in wave conditions is important for prediction of coastal hazards into the future. Deep-water waves from Chapter 2 were shadowed, refracted, diffracted, shoaled, and dissipated over the Southern California Bight bathymetry by a numerical wave model. Results indicate that alongshore variability is strongly governed by bathymetry. Neighboring parts of the coast are sensitive to different atmospheric patterns, which has implications for coastal hazards with the evolution of the atmosphere under climate change.

Use of the improved statistical method described in Chapter 2 yields relatively small errors between nearshore waves predicted in Chapter 3 and wave buoy observations. Yet, discrepancies between modeled and observed wave directions truly limit our ability to use these results for accurate prediction of coastal erosion into the future, as it is sensitively dependent on small shifts in incident wave directions. These results are useful for coastal flooding estimates and for broad prediction of vulnerability by the relative change between historical projections and future projections, as opposed to historical observations and future projections.

Lastly, in Chapter 4, I shift focus to estuarine environments, which are vulnerable as a result of intensive human alteration, sea level rise, and changes to sediment supply. Tidal flow past a small, shallow embayment adjacent to a long, linear estuary is explored using an idealized numerical model. The embayment radius is less than the channel width. Two mechanisms, tidally-driven eddies and the response of the bay to the free surface elevation of the channel, result in the an anomalously salty embayment relative to the adjacent channel. The barotropic pressure gradient is balanced by large across-channel advective flux divergence, which drives salt fluxes across the mouth of the embayment. With variations in the embayment radius, while maintaining that it is smaller than the channel width, the salinity anomaly persists. However, for the radii considered here, the embayment radius and the magnitude of the salinity anomaly appear to have an inverse relationship due to weakening of the barotropic pressure gradient with larger bay radii. The mechanisms identified in this work are likely also responsible for sediment fluxes into and out of some estuarine embayments. Knowledge of embayment circulation patterns aids in restoration and erosion-mitigation efforts focused on sediment accumulation, contaminant removal, or ecosystem health.

Extensive sensitivity studies of the embayment circulation to factors including stratification, embayment depth, rotation, and mixing schemes are necessary and will be pursued in the future. In many estuarine embayments, local wind forcing and Coriolis forcing are important drivers of along- and across-channel circulation, though neither were considered in this work for simplicity. It is important to identify the parameter space in which the mechanisms identified here dominate over others, leading to the observed salt and sediment fluxes. Lastly, the sensitivity of the circulation to embayment radii larger than the channel width was not explored. Though embayments of the spatial scale studied here are common features in estuarine systems, large embayments of the same scale as the channel width or larger are also common and likely are dominated by different mechanisms.

Although Chapters 2 and 3 are implemented in California's coastal systems, the methods used are applicable to complex coastal systems around the world. Improved statistical downscaling methods yield rapid proliferation of robust future wave predictions across all ocean basins. Hybrid statistical-dynamical approaches for the simulation of nearshore waves provide both the efficiency of exclusively statistical methods and the full physics of a purely dynamical method. The investigation of tidal flow past an idealized estuarine embayment is applicable to small, shallow embayments around the world.